Journal of Glaciology

Article

Cite this article: Coffey NB, Lai C-Y, Wang Y, Buck WR, Surawy-Stepney T, Hogg AE (2024). Theoretical stability of ice shelf basal crevasses with a vertical temperature profile. *Journal of Glaciology* 1–22. https://doi.org/10.1017/jog.2024.52

Received: 8 February 2024
Revised: 10 June 2024
Accepted: 13 June 2024

Keywords:
calving; crevasses; ice shelves

Corresponding author:
Niall Bennet Coffey;
Email: nbcoffey@stanford.edu

cambridge.org/jog

Theoretical stability of ice shelf basal crevasses with a vertical temperature profile

Niall Bennet Coffey[1,2], Ching-Yao Lai[1,2,3], Yongji Wang[1,3,4], W. Roger Buck[5], Trystan Surawy-Stepney[6] and Anna Elizabeth Hogg[6]

[1]Department of Geophysics, Stanford University, Stanford, CA, USA; [2]Program in Atmospheric and Oceanic Sciences, Princeton University, Princeton, NJ, USA; [3]Department of Geosciences, Princeton University, Princeton, NJ, USA; [4]Department of Mathematics, New York University, New York, NY, USA; [5]Lamont-Doherty Earth Observatory of Columbia University, New York, NY, USA and [6]School of Earth and Environment, University of Leeds, Leeds, UK

Abstract

Basal crevasses threaten the stability of ice shelves through the potential to form rifts and calve icebergs. Furthermore, it is important to determine the dependence of crevasse stability on temperature due to large vertical temperature variations on ice shelves. In this work, considering the vertical temperature profile through ice viscosity, we compare (1) the theoretical crack depths and (2) the threshold stress causing the transition from basal crevasses to full thickness fractures in several fracture theories. In the Zero Stress approximation, the depth-integrated force at the crevassed and non-crevassed location are unbalanced, violating the volume-integrated Stokes equation. By incorporating a Horizontal Force Balance (HFB) argument, recent work showed analytically that the threshold stress for rift initiation is only half of that predicted by the Zero Stress approximation. We generalize the HFB theory to show that while the temperature profile influences crack depths, the threshold rifting stress is insensitive to temperature. We compare with observations and find that HFB best matches observed rifts. Using HFB instead of Zero Stress for cracks in an ice-sheet model would substantially enlarge the predicted fracture depth, reduce the threshold rifting stress and potentially increase the projected rate of ice shelf mass loss.

1. Introduction

Basal crevasses, which are vertical fractures on the underside of ice, can play an important role in the calving process and thus the stability of ice shelves and marine-terminating glaciers (McGrath and others, 2012a; Colgan and others, 2016; Jeong and others, 2016). A reduction in buttressing through calving or other processes can increase the mass loss from ice sheets and raise global mean sea level by increasing the grounding line flux (Thomas and MacAyeal, 1982; Rott and others, 2002; Rignot and others, 2004; Dupont and Alley, 2005; Pritchard and others, 2012; Haseloff and Sergienko, 2018). Individual basal crevasses can induce surface crevasses, create surface depressions when sufficiently deep that may enable surface meltwater ponding, reduce the ability of ice shelves to provide back stress to upstream grounded ice and penetrate through the full ice thickness to form rifts (Pralong and Funk, 2005; McGrath and others, 2012b; Luckman and others, 2012; Child and others, 2021). When spaced periodically, basal crevasses can potentially stabilize ice shelves from breakup through dampening stresses transmitted through high-frequency elastic-flexural waves (Freed-Brown and others, 2012). The evolution of basal crevasses has been modeled by the balance of ice shelf and hydrostatic ocean stresses (Zarrinderakht and others, 2022), as well as idealized ocean dynamics and the mass balance of melting and freezing (Jordan and others, 2014). Basal crevasses may play a central role in the flexure-driven calving of marine-terminating glaciers seen in Greenland and Canada (Wagner and others, 2014; Murray and others, 2015; Wagner and others, 2016; Benn and others, 2017). In Antarctica, basal crevasses may initiate rifts (Jeong and others, 2016; Joughin and others, 2021) that can propagate across the ice shelf and calve icebergs (Lipovsky, 2020). These icebergs can transport fresh meltwater equatorwards and threaten biodiversity of islands in the Southern Ocean (Huth and others, 2022).

While the calving of icebergs is likely caused by multiple mechanisms, we focus on the transition from basal crevasses to full-thickness fractures, also referred to as rifts. In the absence of ample surface meltwater such as surface melt ponds, basal crevasses are theoretically more vulnerable than surface crevasses to full-thickness penetration and cause rift initiation (Lai and others, 2020). The depth-averaged deviatoric stress formulations of Nye (Nye, 1955), Weertman (Weertman, 1973) and the zero toughness or half-space formulations of Mode I Linear Elastic Fracture Mechanics (LEFM) (van der Veen, 1998a) all predict basal crevasses to be about nine times deeper than dry (water-free) surface crevasses. The magnitude of lithostatic stress only decreases as basal crevasses propagate upwards, yet increases as surface crevasses propagate downwards, making the initiation of rifts more likely due to basal crevasses than dry surface crevasses. Thus, we study basal crevasses as the precursors of rifts in the absence of strong atmospheric forcing (Morris and Vaughan, 2003; van Wessem and others, 2023).

https://doi.org/10.1017/jog.2024.52 Published online by Cambridge University Press

Driven by the importance to predict rift initiation on ice shelves, here we extend analytical and numerical models to both predict the ice shelf threshold stress R^*_{xx} for rifts to initiate from Mode I (tensile) basal crevasses, and include a vertical temperature profile, which we show can substantially affect fracture predictions, yet is currently neglected in fracture parameterization in ice-sheet models (Goelzer and others, 2020; Seroussi and others, 2020). We consider three theories for Mode I basal crevasses to propagate into rifts: (1) the Zero Stress approximation (Jezek, 1984; Benn and others, 2007; Nick and others, 2010), (2) LEFM for basal crevasses (van der Veen, 1998a; Tada and others, 2000; Lai and others, 2020) and (3) the Horizontal Force Balance (HFB) (Buck, 2023). On ice shelves, the Zero Stress approximation forms rifts from the intersection of basal crevasses with a surface crevasse, and requires the largest amount of tensile stress among the three theories for a rift to form. LEFM considers an isolated basal crevasse such that stress can concentrate at the crack tip and predicts the smallest amount of tensile stress required for rift initiation. The major limitation of current LEFM-based basal crevasse theory used in this paper (van der Veen, 1998a) is its neglection of the restoring force at the deformed ice-ocean interface, leading to non-physical predictions of the rifting stress. The HFB theory considers the union of surface and basal crevasses for rift formation in a material with zero strength, similar to the Zero Stress approximation. However, unlike the Zero Stress approximation, HFB theory does not violate static force balance. We find that the rifting stress predicted by HFB for a range of temperature profiles is the same as the tensile stress at the ice shelf front with no sea ice buttressing; a rifting stress slightly greater than that of LEFM but much less than that of the Zero Stress approximation.

Our fracture models' deviations from standard implementations and validation of the Zero Stress approximation (Jezek, 1984; Benn and others, 2007; Nick and others, 2010) and Mode I LEFM for basal crevasses (van der Veen, 1998a) are summarized below. First, we include the depth variation of the resistive stress R_{xx} due to vertical temperature variation in all theories and compare the results. We chose a linear temperature profile for simplicity, and then show the effects of a different temperature profile. Second, we enforce the Zero Stress approximation to uphold HFB and include vertical temperature variations, following a procedure similar to Buck (2023) and obtaining a simple analytical result. Third, we shift the focus from crevasse depth prediction to rift formation prediction, analyzing results in terms of stress required for basal crevasses to unstably propagate and initiate rifts or calving events. Fourth, we validate rift formation predictions with an existing rift catalog (Walker and others, 2013) on the Ross Ice Shelf (RIS) and Larsen C Ice Shelf (LCIS). We verified that the deviation in resistive stress between the 1D fracture theory and the 2D Shallow-Shelf Approximation (SSA) (MacAyeal, 1989) is less than 10%, thus ensuring validity of the 1D flow assumption in the regions of interest.

2. Fracture models of basal crevasses with vertically varying ice temperature

The basal crevasse evolution problem is illustrated schematically in Figure 1a, where crack growth may either terminate at a stable length, or propagate unstably to form a rift, with outcome subject to the chosen fracture theory. Figure 1b shows the differences between existing isothermal basal crevasse depth prediction theories: the Zero Stress approximation, LEFM and a new HFB model in (Buck, 2023). While these theories differ for a range of crack depths, the largest discrepancy is near the sea level, where basal crevasses can unstably propagate and form rifts. Although the basal crevasse to rift transition is challenging to precisely measure given the current spatiotemporally sparse observations (see Appendix B), Figure 1c through f motivates our study of rift initiation associated with basal crevasse vertical propagation through observed increases in resistive stress upon rift formation. Importantly, ice shelves are not isothermal, and basal crevasse depths are sensitive to the ice shelf vertical temperature profile (Rist and others, 2002; Borstad and others, 2012; Lai and others, 2020). We analyze several fracture models (van der Veen, 1998a; Nick and others, 2010; Buck, 2023) and the stress required to form rifts, considering a vertically linear temperature profile for simplicity. We assume that the base of the ice shelf is held at $T_b = -2$ °C, and take a linear temperature profile up to the surface temperature T_s as predicted by RACMO (van Wessem and others, 2018). To conclude this section, we show that having a Robin temperature profile (Robin, 1955) does not change the results of this study.

The historical focus on crevasses was centered on surface crevasses, with Nye's Zero Stress (Nye, 1955) and LEFM (Smith, 1976). However, the use of radar confirmed the presence of crevasses extending upwards from the bottom of the ice (Jezek and others, 1979; Jezek and Bentley, 1983). The surface crevasses theories were later extended to study basal crevasses (Jezek, 1984; Benn and others, 2007; Nick and others, 2010; van der Veen, 1998a). The Zero Stress approximation we refer to in this paper considers these extensions (Jezek, 1984; Benn and others, 2007; Nick and others, 2010) of Nye's Zero Stress approximation that consider both a surface crevasse and a hydrostatic seawater pressure inside a basal crevasse.

Since the setup of these basal crevasse depth theories share many basic assumptions, we will first present the commonalities, and then explore each individually. As shown in Figure 1a, given a 2D coordinate system with x as the horizontal dimension and z as the vertical dimension, assuming incompressibility and a stress-free upper surface, we can write the net longitudinal stress σ_n of van der Veen (1998a) at the approximately vertical basal crevasse interface as

$$\sigma_n(z) = R_{xx}(z) - p_l(z) + p_w(z), \tag{1}$$

where $R_{xx}(z)$, $p_l(z)$ and $p_w(z)$ are the along-flow component of ice shelf resistive stress defined in Cuffey and Paterson (2010), ice lithostatic pressure and hydrostatic water pressure, respectively. As in the Shallow Shelf Approximation of Stokes flow (MacAyeal, 1989), we assume that there is negligible vertical shear stress in the ice due to negligible shear stress on the surface and basal boundaries. By setting $z = 0$ at the ice shelf base and positive upwards as shown in Figure 1a, we define the pressure terms as $p_l = \rho_i g\ (H - z)$ and water pressure $p_w = \rho_w g\ \max(z_h - z,\ 0)$, with gravitational acceleration $g = 9.8$ m s^{-2}, vertically integrated ice density $\rho_i = 917$ kg m^{-3} and ice thickness H. The piezometric head $z_h = H\rho_i/\rho_w$ as defined in Nick and others (2010) depends on the water density; for this study, we assume constant saltwater density $\rho_w = 1028$ kg m^{-3}.

The way that we account for vertical temperature profile $T(z)$ is through the ice hardness $B(T)$ in the effective viscosity. Modeling ice as a Non-Newtonian power-law fluid (Glen, 1958), the effective viscosity is,

$$\mu = \frac{B(T)}{2}\dot{\epsilon}_e^{(1/n)-1} \approx \frac{B(T)}{2}\dot{\epsilon}_{xx}^{(1/n)-1}, \tag{2}$$

where the effective strain rate $\dot{\epsilon}_e = \sqrt{\dot{\epsilon}_{ij}\dot{\epsilon}_{ji}/2}$, i.e. the second invariant of the strain rate tensor $\dot{\epsilon}_{ij}$, is dominated by the along-flow component $\dot{\epsilon}_{xx}$ in comparison to the across-flow and shear terms. Denoting τ_{xx} as the along-flow component of the deviatoric stress, the along-flow resistive stress $R_{xx} = 2\tau_{xx} = 4\mu\dot{\epsilon}_{xx}$ can be

https://doi.org/10.1017/jog.2024.52 Published online by Cambridge University Press

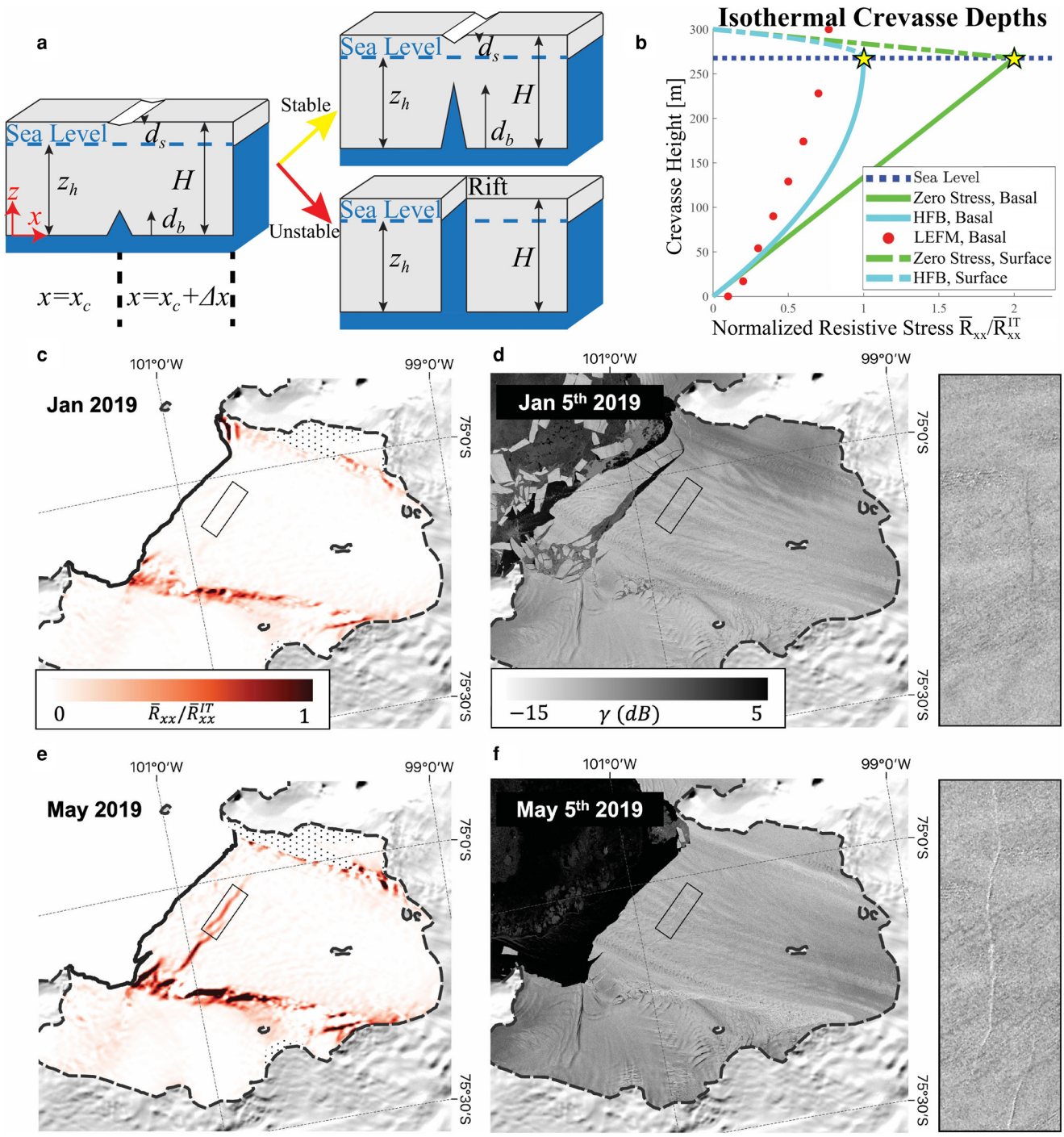

Figure 1. (a) Schematic of crevasses propagating stably or unstably and forming a full-thickness fracture called a rift. Crevasse depths d_s, d_b, thickness H, coordinate system and piezometric head at sea level z_h are illustrated. (b) Several previously existing isothermal crevasse depth predictions versus depth-averaged resistive stress $\bar{R}_{xx}$ normalized by the analytical depth-averaged ice tongue resistive stress $\bar{R}^{IT}_{xx}$ for $H = 300$ m. Circular red dots are LEFM basal crevasse depth numerical predictions, solid lines are basal crevasse depth analytical theory and dash-dotted lines are surface crevasse depth analytical theory. Rifts initiate either where $d_b = H$ for LEFM or at the stars that denote the intersection of surface and basal crevasse tips. Horizontal Force Balance (HFB) and Zero Stress require the existence of both surface and basal crevasses on ice shelves for theoretical consistency, whereas LEFM treats an isolated basal crevasse. Subfigures (c) to (f) show a potential instance of the basal crevasse-to-rift transition (Jeong and others, 2016; Joughin and others, 2021) over Pine Island Ice Shelf during January to May 2019. (c) An estimate of the ratio $\bar{R}_{xx}/\bar{R}^{IT}_{xx}$ over Pine Island Ice Shelf found using ice velocity data averaged over the month of January 2019 (Wuite and others, 2021). (d) SAR backscatter image at 50 m resolution from 5th January 2019, and a close-up showing the terminus region of Pine Island Ice Shelf where a fracture (can be surface crack, surface expression of basal crack or rift) is dimly visible. (e) The equivalent of (c) for May 2019. (f) A backscatter image from May 2019 where a rift is clearly visible. Grounded ice (Haran and others, 2013), grounding lines (Mouginot and others, 2017b) and calving fronts are denoted by masking, a dashed black line and a solid black line, respectively.

written as

$$R_{xx} = 2B(T)\dot{\epsilon}_{xx}^{1/n}. \tag{3}$$

Based on lab experiments, the Glen's flow law gives $n = 3$ (Glen, 1958), and $B(T)$ (LeB Hooke, 1981) can be expressed as

$$B(T) = B_0 \exp\left[\frac{T_0}{T} - \frac{C}{(T_r - T)^k}\right], \tag{4}$$

https://doi.org/10.1017/jog.2024.52 Published online by Cambridge University Press

where $B_0 = 2.207$ Pa · yr$^{1/n}$, $T_0 = 3155$ K, $T_r = 273.39$ K, $k = 1.17$ and $C = 0.16612$ K^k are constants determined from empirical fit (LeB Hooke, 1981). We discuss sensitivity to rheology choices in the Robin Temperature Profile subsection, the Discussion and Conclusions section, and Appendix F.

2.1. Zero stress approximation

Nye's theory (Nye, 1955) assumes that a crevasse will stop propagating when further infinitesimal crack growth would put the net longitudinal stress σ_n at the crack tip into compression. Originally conceived for surface crevasses only, it has been extended to model basal crevasses by approximating the stress exerted from the ocean on crevasse walls as hydrostatic (Jezek, 1984; Benn and others, 2007; Nick and others, 2010; Duddu and others, 2020). This so-called Zero Stress approximation generates crevasses where there is net tensile stress; on ice shelves, surface and basal crevasses are both allowed to propagate. While previous Zero Stress applications assume isothermal ice (Nye, 1955; Jezek, 1984; Benn and others, 2007; Nick and others, 2010; Duddu and others, 2020), we have extended the theory to consider depth-varying temperature. As derived in Appendix C, a basal crevasse on a freely floating ice shelf with vertical temperature variation can unstably propagate to the surface when the resistive stress is above the threshold

$$\frac{\bar{R}_{xx}}{\bar{R}_{xx}^{IT}} \geq 2\frac{\rho_w}{\rho_i}\frac{d_b^*}{H}\frac{\overline{\tilde{B}(T)}}{\tilde{B}\left(T\left(d_b^*/H\right)\right)}, \tag{5}$$

where the overline $\bar{q}$ represents a depth-averaged value for the variable q. The dimensionless numbers involved are the ratio of densities ρ_w/ρ_i; the unstable basal crevasse depth d_b^* relative to ice thickness H; the non-dimensional ice hardness $\tilde{B}(T) \equiv B(T)/B(T(z=0))$; and the non-dimensional ice hardness at the unstable basal crevasse depth $\tilde{B}(T(d_b^*/H))$; the depth-averaged resistive stress $\bar{R}_{xx}$ relative to the resistive stress of a 1D unbuttressed ice tongue $\bar{R}_{xx}^{IT} \equiv \left(1-\rho_i/\rho_w\right)\rho_i g H/2$ as derived by Weertman (1957) from the force balance for an ice tongue $\int_0^H R_{xx}(z)\mathrm{d}z = \int_0^H 4\mu\dot{\epsilon}_{xx}\mathrm{d}z = \left(1-\rho_i/\rho_w\right)\rho_i g H/2$. In the Zero Stress approximation, all basal crack depths less than the unstable basal crevasse depth d_b^* are stable, while those greater than or equal to d_b^* will result in rift formation.

As shown in Appendix C, we write the result of depth-dependent resistive stress in terms of depth-averaged resistive stresses such that we can use the same ratio $\bar{R}_{xx}^*/\bar{R}_{xx}^{IT}$ between all theories in this paper. Note that when we treat the ice as isothermal or utilize a depth-averaged resistive stress instead of the depth-varying resistive stress, the ice hardness ratio $\overline{\tilde{B}(T)}/\tilde{B}(T(d_b^*/H))$ is 1, and the maximum basal crevasse depth is from the base to sea level $\left(\rho_w d_b^*\right)/\left(\rho_i H\right) = 1$, making the right-hand side of Eqn (5) equal to 2. Thus, under the Zero Stress approximation, a basal crevasse will propagate to the sea level, intersecting a surface crevasse to form a rift in isothermal ice when the depth-averaged resistive stress is twice that of an isothermal ice tongue, as shown in Figure 1b.

The simplicity of the Zero Stress approximation comes with limitations. The rifting stress threshold we derived in Appendix C to get Eqn (5) does not include stress concentration near crack tips, the material strength of ice, accumulation and melt, nor crevasse-induced stresses in ice. The lack of stress concentration and zero material strength is applicable in the limit of closely spaced crevasses (De Robin, 1974; Weertman, 1974), where the spacing between crevasses is much less than the individual crevasse depths (Weertman, 1977). Observations indicate basal crevasse spacing to be roughly one to several ice thicknesses (Luckman and others, 2012; McGrath and others, 2012a; Lawrence and others, 2023), breaking the densely spaced crevasses assumption. Recent extensions of the Zero Stress approximation include non-zero material strength (Benn and others, 2007) and accumulation and melting effects (Bassis and Ma, 2015; Huth and others, 2021). In the limit of densely spaced crevasses with negligible flexural stress, the effects of crevasse-induced stress on crack depth has been included to satisfy a HFB argument (Buck, 2023). We present an approach to generalize this approximate crevasse-induced stress for vertically varying ice temperature in the Horizontal force balance section.

2.2. Linear elastic fracture mechanics

In contrast to the Zero Stress approximation, the LEFM framework, first applied to surface crevasses by Smith (1976) and later applied to basal crevasses by van der Veen (1998a), considers an isolated basal crevasse with stress concentration near the crack tip and assumes small-scale yielding (Zehnder, 2012). It has been shown that LEFM agrees with the analytical approach of including stress concentration near crack tips by Weertman (1973) for small crack depths (Buck and Lai, 2021). Unlike Weertman's infinite thickness assumption (Weertman, 1973), LEFM comes with the advantage of accounting for a prescribed finite thickness (van der Veen, 1998a). The LEFM rifting threshold $\bar{R}_{xx}^*$ for an isothermal ice shelf with traction-free upper and lower surfaces has been reported by Zarrinderakht and others (2022) and Lai and others (2020). Building on previous work (van der Veen, 1998a; Tada and others, 2000; Lai and others, 2020), we extended the LEFM analysis across a range of surface temperatures applicable to Antarctica and present the rifting threshold $\bar{R}_{xx}^*$ for a vertically varying ice temperature.

The criterion for Mode I (tensile) crevasse propagation in LEFM is that a crack can propagate so long as the stress intensity factor K_I is at least as large as the fracture toughness K_{Ic}, $K_I \geq K_{Ic}$. Following Tada and others (2000); van der Veen (1998a); Lai and others (2020), the stress intensity factor for a Mode I basal crack can be written as

$$K_I = \int_0^{d_b} \frac{2\sigma_n(z)}{\sqrt{\pi d_b}} \frac{G(\zeta, \tilde{d}_b)}{\left(1-\tilde{d}_b\right)^{3/2}\left(1-\zeta^2\right)^{1/2}}\mathrm{d}z, \tag{6}$$

where d_b is basal crack depth, H is ice thickness, $\zeta \equiv z/d_b$ is a dimensionless height that is one at the crack tip, $\tilde{d}_b \equiv d_b/H$ is the dimensionless basal crack depth relative to the ice thickness, σ_n is the net longitudinal stress defined in Eqn (1), and $G(\zeta, \tilde{d}_b)$ is a dimensionless weight function given by Tada and others (2000) (page 71) which is 99% accurate for any crack depth d_b. For the fracture toughness of glacial ice, we use the experimental value of $K_{Ic} = 150$ kPa$\sqrt{\text{m}}$, which is found to be independent of temperature (Litwin and others, 2012). For rifting, we follow the non-dimensionalization and stability criteria in the Supplemental material of Lai and others (2020): rifts are formed from unstable basal cracks when the tensile stress is large enough such that $\tilde{K}_I \equiv K_I/\rho_i g H^{3/2}$ increases monotonically with $\tilde{d}_b$ (see Fig. 13). One caveat is the assumption that the ice includes pre-existing initial flaws with size d_b^i, which depends on the stress state, thickness and fracture toughness. The theoretical estimates of d_b^i are 3 orders of magnitude smaller than the ice thickness for $H = 300$ m, as discussed in Appendix D, and thus one would expect the existence of these pre-existing flaws.

We can approximately explain the dependence of rifting stress on ice temperature by extending a torque equilibrium argument by Zarrinderakht and others (2022) with isothermal ice to

https://doi.org/10.1017/jog.2024.52 Published online by Cambridge University Press

account for the temperature structure effects. As in Appendix C of Zarrinderakht and others (2022), the rifting stress threshold can be determined by zero torque (or moment) into the page associated with a deep basal crevasse. Mathematically,

$$\tau_y = \hat{y}\cdot\left(\underline{r}\wedge\underline{F}\right) = 2\int_b^s \left(R_{xx}(z)-\rho_i g(s-z)\right)(s-z)\mathrm{d}z - 2\int_b^0 \rho_w g z(s-z)\mathrm{d}z = 0, \quad (7)$$

where s and b are the freely floating ice surface and base, the origin $z=0$ is at sea level, and the ocean restoring force due to the vertically deformed ice-ocean interface is neglected for equivalent comparison. The only difference from Zarrinderakht and others (2022) is the depth-variation of the resistive stress due to temperature $R_{xx}(z)$. For simplicity, we approximate the ice hardness function in Eqn (4) with B_a in Eqn (E8) (see Fig. 2a),

$$B_a(T(\tilde{z})) \approx B_0 \exp\left[\frac{T_0}{T_b}\right]\exp\left[\frac{\tilde{z}+\frac{\rho_i}{\rho_w}}{\tilde{z}_0}\right], \quad (8)$$

with $\tilde{z}=z/H=0$ at sea level, constants $B_0 = 2.207\ \mathrm{Pa}\cdot\mathrm{yr}^{1/n}$, $n=3$, $T_0 = 3155$ K, surface temperature T_s, basal temperature T_b and the dimensionless e-folding length scale assuming a linear temperature profile $\tilde{z}_0 \equiv ((T_0/T_b)(1-T_s/T_b))^{-1}$. Computation of the moments with vertical temperature structure as in (7) were also presented in Buck (2024). Substituting (8) into the resistive stress (3) and calculating the torque equilibrium (7), the temperature-structure-dependent LEFM rifting stress threshold can be analytically derived,

$$\frac{\bar{R}^*_{xx}}{\bar{R}^{IT}_{xx}} = \frac{\frac{2}{3}\left(2-\frac{\rho_i}{\rho_w}\right)}{2\tilde{z}_0\left(1-\left(\tilde{z}_0\left(\exp\left(\frac{1}{\tilde{z}_0}\right)-1\right)\right)^{-1}\right)}. \quad (9)$$

The numerator of the equation is the same as that in Zarrinderakht and others (2022), while the denominator is the contribution due to a linear temperature profile. While this equation is based on an approximate ice hardness function, it approximately explains the numerical LEFM solution (see Fig. 2b), capturing the role of linear vertical temperature dependence through one new dimensionless variable, the dimensionless e-folding length scale $\tilde{z}_0$. Figure 2b shows that the dimensionless LEFM rifting stress threshold decreases with warmer surface temperature, consistent with Figure 4c.

One of the largest limitations of this version of LEFM is neglecting the oceanic restoring force associated with the vertical displacement at the ice-ocean boundary (Jimènez and Duddu, 2018; Huth and others, 2021; Zarrinderakht and others, 2022), which is expected to be particularly important for deep basal crevasses. Accounting for this oceanic restoring force in a LEFM framework is the subject of future work. However, the effect of buoyancy is included in the numerical simulations of an isolated basal crevasse in Buck and Lai (2021), which predicts the same rifting stress threshold as the HFB theory presented in the next section.

2.3. Horizontal force balance

In the standard Zero Stress approximation, the depth-integrated horizontal force per unit width (F_x) at the crevassed ($x=x_c$) and non-crevassed location ($x=x_c+\Delta x$) are unbalanced (see Figs 3b,d). If this force is unbalanced ($\sum F_x \neq 0$), according to the Newton's Second Law this net force acting on the ice in the control volume enclosed by the black dashed lines in Figure 3a should lead to acceleration of the ice masses, which is inconsistent with our Stokes flow assumption. The main assumption in the Zero Stress approximation that led to the inconsistency is the neglection of crevasse-induced stresses in the unbroken ligament between the surface and basal crevasse tips (Figs 3a,b). Recent work by Buck (2023) shows a new model that includes the crevasse-induced stresses in the unbroken ice (Fig. 3c) by incorporating a HFB argument. In this section, we apply the same argument for an ice shelf with vertically varying temperature. We use an Eulerian control volume approach (the box enclosed by the black dashed lines in Fig. 3a). Note that by satisfying HFB we mean that the total force acting on the control volume argument is zero ($\sum F_x = 0$), satisfying Newton's Second Law. As assumed

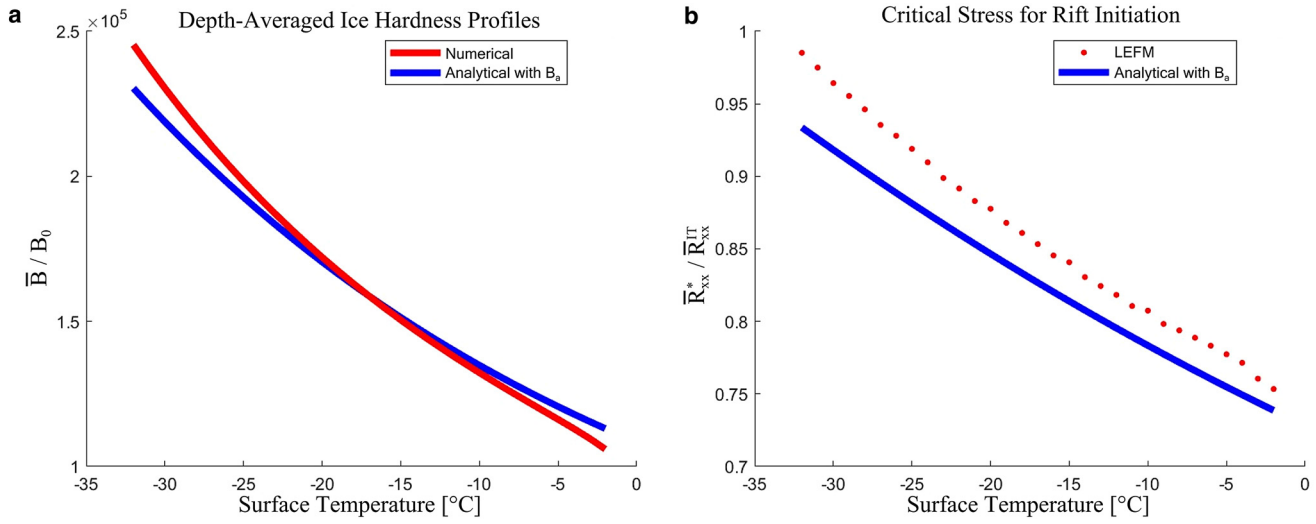

Figure 2. (a) Comparison of depth-averaged ice hardness value $\bar{B}$ normalized by the constant B_0 from LeB Hooke (1981) versus surface temperature, assuming a linear temperature profile. The red curve numerically integrates (4), while the blue curve is an analytical integral of the approximated ice hardness profile B_a (8). (b) Comparison of the rifting stress threshold versus surface temperature, assuming a linear temperature profile. The LEFM numerical solution calculated using (6) is shown with red dots, while the analytical solution (9) based on torque equilibrium with an approximated ice hardness B_a (8) is in solid blue. We plot the limit of $T_s \longrightarrow -2$ °C for the rifting stress from torque equilibrium as it converges to the isothermal case. The difference between the analytical and numerical results is non-negligible, thus for the rest of the paper we use the numerical LEFM results. That said, the analytical result (9) offers interpretable insight by capturing the role of the linear temperature profile with one additional dimensionless variable, the e-folding length scale $\tilde{z}_0$.

https://doi.org/10.1017/jog.2024.52 Published online by Cambridge University Press

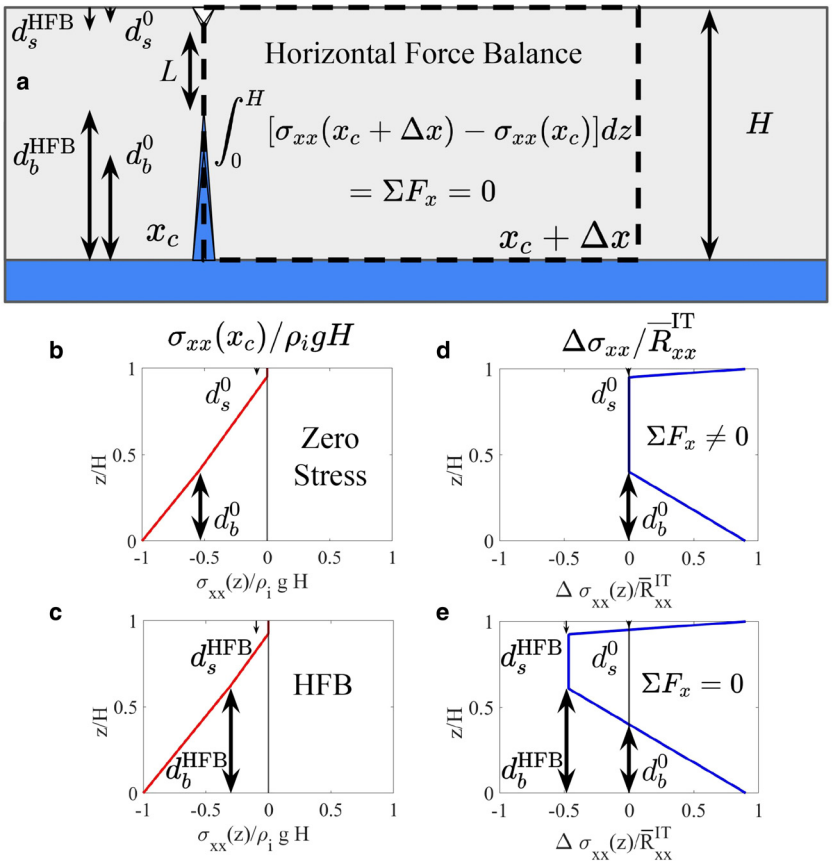

Figure 3. (a) Schematic showing force balance between a downstream, unperturbed location $x = x_c + \Delta x$ and the crevassed location at $x = x_c$ with crevasse depths, surface d_s and basal d_b. The unbroken ligament is depicted of length $L = H - d_s - d_b$. The unperturbed background longitudinal stress at $x = x_c + \Delta x$ in this example is $\sigma_{xx}(x_c + \Delta x) = R_{xx} - p_i = 0.9\overline{R}_{xx}^{IT} - \rho_i g(H - z)$. For the remaining subfigures, the top and bottom row correspond to the Zero Stress approximation and HFB (Buck, 2023), respectively. Figures (b) and (c) show the longitudinal stress profiles normalized by $\rho_i g\ H$ at the crevassed location in the Zero Stress approximation and HFB (Buck, 2023). Figures (d) and (e) correspond to the stress difference profiles $\Delta\sigma_{xx} \equiv \sigma_{xx}(x_c + \Delta x) - \sigma_{xx}(x_c)$ normalized by $\overline{R}_{xx}^{IT}$. The Zero Stress approximation does not uphold force balance because the stress difference is positive or zero for all depths, yet HFB is defined to uphold the horizontal force balance constraint as written in (a). We include crack depths for the Zero Stress approximation, where the blue curve intersects zero and labeled with the superscript 0, as well as the deeper HFB crack depths labeled with the superscript HFB.

in the Zero Stress approximation, we consider the limiting case of a densely crevassed ice shelf where flexural stresses are negligible.

Our fixed control volume in Figure 3 has vertical boundaries at the ice shelf surface and base, and horizontal boundaries at the symmetry plane of a basal crevasse, $x = x_c$, and at a nearby downstream location $x = x_c + \Delta x$ with the same ice thickness. The temperature profile that dictates the vertical profile of $R_{xx}(T(z))$ is depicted in Figure 1. We start with Stokes flow, yet inertial terms may be non-negligible (Bassis and Kachuck, 2023). Taking glaciostatic balance as in Lindstrom and MacAyeal (1987) as the vertical force balance,

$$\partial_z \sigma_{zz} = \rho_i g, \tag{10}$$

we integrate from a level z to the surface H, i.e. $\sigma_{zz} = \rho_i g\ (z - H)$, and solve for pressure

$$p(z) \equiv -\sigma_{zz} + \tau_{zz} = \rho_i g(H - z) + \tau_{zz} \tag{11}$$

using a stress-free upper surface boundary condition. From the downstream side of the control volume at $x = x_c + \Delta x$, the longitudinal ice shelf Cauchy stress can be written as

$$\begin{aligned}\sigma_{xx}(x_c + \Delta x, z) &\equiv -p + \tau_{xx} = -\rho_i g(H - z) - \tau_{zz} + \tau_{xx} \\ &= -\rho_i g(H - z) + R_{xx}(z),\end{aligned} \tag{12}$$

where the deviatoric stress tensor $\tau_{ij} = \sigma_{ij} + p\delta_{ij}$ by definition has zero trace tr $(\tau_{ij}) = 0$ (e.g. see Section 12.1 of Rudnicki (2014)), and thus $\tau_{xx} = -\tau_{zz}$ in a 2D $(x,\ z)$ system without assuming incompressibility. Note that this stress distribution (12) is valid for an uncrevassed location, where there is no basal crevasse-induced flexural stress.

At $x = x_c$, in order to satisfy HFB ($\sum F_x = 0$), the extra compressive stresses in the unbroken ligament of length L between the surface and basal crevasse tips, induced by the crevasses themselves, need to be considered. We parameterize this crevasse-induced stress to satisfy three conditions:

1. the zero material strength assumption of the Zero Stress approximation (Nye, 1955; Jezek, 1984; Benn and others, 2007; Nick and others, 2010),
2. continuity of stress at crack tips (Buck and Lai, 2021) and
3. HFB (Buck, 2023).

Previous zero stress models (Nye, 1955; Benn and others, 2007; Nick and others, 2010; Duddu and others, 2020) use condition 1 to solve for crack depth; we maintain that the stress field obey condition 3 for static equilibrium, and take conditions 1 and 2 in the limit of a densely crevasses ice shelf with negligible flexural stresses.

The longitudinal stress that is consistent with conditions 1 and 2 can be written in a piecewise fashion corresponding to a dry surface crevasse of depth d_s $(H - d_s \le z \le H)$, a water-filled basal crevasse of depth d_b $(0 \le z \le d_b)$ and an ice ligament between the two $(d_b \le z \le H - d_s)$,

$$\sigma_{xx}(x_c, z) = \begin{cases} 0, & H - d_s \le z \le H \quad \text{(surface crevasse)} \\ -\rho_i g(H - z) + cR_{xx}(z), & d_b \le z \le H - d_s \quad \text{(unbroken ice)} \\ -\rho_w g(z_h - z), & 0 \le z \le d_b \quad \text{(basal crevasse).} \end{cases} \tag{13}$$

Here, $cR_{xx}(z)$ represents the sum of the background resistive stress and the crevasse-induced compressive stress in the unbroken ice ligament, $d_b \le z \le H - d_s$.

https://doi.org/10.1017/jog.2024.52 Published online by Cambridge University Press

We note that while a precise numerical profile of the stresses in the ice ligament can differ from the parameterized form cR_{xx}, the deviation would be negligible in the limit of a very small unbroken ice ligament and so the rifting stress threshold will be accurate despite the parameterized stress profile (13). Investigations of material strength effects, crevasse-induced flexural stresses and more complicated physical descriptions of the stress within the unbroken ice ligament are subjects for future work.

HFB on an Eulerian or fixed control volume, defined with negligible inertial term as the Stokes equation, can be written as

$$0 = \int_0^H \int_{x_c}^{x_c+\Delta x} [\partial_x \sigma_{xx} + \partial_z \tau_{zx}] \mathrm{d}x \mathrm{d}z. \tag{14}$$

The negligible shear stress on the upper and lower surfaces simplifies Eqn (14) such that the sum of the horizontal forces per unit width into the page on our control volume is zero,

$$\int_0^H [\sigma_{xx}(x_c + \Delta x) - \sigma_{xx}(x_c)] \mathrm{d}z = 0. \tag{15}$$

Solving for the constant, c, in Eqn (13) and finding a relation between surface and basal crack depths will close the system of equations, allowing us to determine crevasse depths given a normalized resistive stress $\bar{R}_{xx}/\bar{R}_{xx}^{IT}$.

2.3.1. Crevasse depths

Following Buck and Lai (2021), we use continuity of stress at crack tips, $z = H - d_s$ and $z = d_b$, as a constraint to determine the constant c and then a relation between the crevasse depths. At the tip of the surface crevasse, we have that

$$0 = -\rho_i g d_s + c(R_{xx})|_{z=H-d_s}, \tag{16}$$

which easily resolves the constant as

$$c = \frac{\rho_i g d_s}{(R_{xx})|_{z=H-d_s}}. \tag{17}$$

At the basal crevasse tip, we have that

$$-\rho_i g H + \rho_w g d_b = -\rho_i g (H - d_b) + \frac{\rho_i g d_s}{(R_{xx})|_{z=H-d_s}} (R_{xx})|_{z=d_b}, \tag{18}$$

which can readily be simplified to a dimensionless relation between basal and surface crack depth,

$$\frac{d_b}{d_s} = \frac{\rho_i}{\rho_w - \rho_i} \frac{B(T|_{z=d_b})}{B(T|_{z=H-d_s})} \quad \text{for the general case.} \tag{19}$$

Thus, the temperature profile $T(z)$ affects the relative surface to basal crevasse depth through $B(T(z))$, with colder surface temperatures creating larger crevasse depth ratio d_s/d_b.

Finally, having solved for the constant, we may now impose the force balance constraint of Eqn (15) with the stress expressions in Eqns (12) and (13). Defining the dimensionless variables $\tilde{d}_b = d_b/H$, $\tilde{d}_s = d_s/H$ and $\tilde{z} = z/H$, the dimensionless force balance can be written as

$$\frac{\bar{R}_{xx}}{\bar{R}_{xx}^{IT}} = \frac{\rho_w}{\rho_w - \rho_i} \tilde{d}_s^2 + \frac{\rho_w}{\rho_i} \tilde{d}_b^2 + \frac{\tilde{d}_s}{\frac{1}{2}\left(1 - \frac{\rho_i}{\rho_w}\right) \tilde{B}\left(T|_{\tilde{z}=1-\tilde{d}_s}\right)} \times \int_{\tilde{d}_b}^{1-\tilde{d}_s} \tilde{B}(T(\tilde{z})) d\tilde{z} \text{ for the general case.} \tag{20}$$

Equations (19) and (20) form a system of two equations with the surface and basal crack depths as the two unknown variables, given that $\bar{R}_{xx}/\bar{R}_{xx}^{IT}$ is known.

For isothermal ice shelves, the ice hardness functions of Eqn (19) become constants as in Eqn (E6), and we have

$$\frac{d_b}{d_s} = \frac{\rho_i}{\rho_w - \rho_i} \quad \text{for the isothermal case.} \tag{21}$$

The equation has an analytical solution (Buck, 2023),

$$\tilde{d}_b = \tilde{d}_s \frac{\rho_i}{\rho_w - \rho_i}, \quad \text{and,} \quad \tilde{d}_b = \frac{\rho_i}{\rho_w}\left(1 - \sqrt{1 - \frac{\bar{R}_{xx}}{\bar{R}_{xx}^{IT}}}\right) \quad \text{for the isothermal case,} \tag{22}$$

which predicts that rifts would form when the background resistive stress reaches that of a freely floating ice shelf without buttressing, i.e. $\bar{R}_{xx}^*/\bar{R}_{xx}^{IT} = 1$. Importantly, we did not set $\bar{R}_{xx}^* = \bar{R}_{xx}^{IT}$; this arises naturally as the force balance solution to rift formation where $\tilde{d}_b + \tilde{d}_s = 1$,

$$\tilde{d}_b + \tilde{d}_s = 1 - \sqrt{1 - \frac{\bar{R}_{xx}}{\bar{R}_{xx}^{IT}}} = 1 \quad \text{for the isothermal rift case.} \tag{23}$$

When we include the vertical temperature profile, we compute the ice hardness function given vertical temperature variation numerically. We iterate through temperature profiles and basal crevasse depths to solve for surface crevasse depth through the equation residual of Eqn (19). Having numerically obtained a relation between $\tilde{d}_b$ and $\tilde{d}_s$, we use these values to solve for $\bar{R}_{xx}/\bar{R}_{xx}^{IT}$ in Eqn (20). We plot dimensionless basal crack depth as a function of $\bar{R}_{xx}/\bar{R}_{xx}^{IT}$ for the linear vertical temperature case in Figure 4. When the crack is stable, the crevasse depth is instantaneously determined by the stress state. This is consistent with the Zero Stress approximation (Benn and others, 2007; Nick and others, 2010) and van der Veen (1998a)'s basal crevasse LEFM consideration of neglecting time-dependent fracture propagation, but is a possible future extension (Lawn, 1993).

2.3.2. Rifting stress

We find that the crevasse to rift transition for cold and warm ice shelf surface temperatures occurs at roughly the same critical stress. Thus, HFB can be approximated by a simple analytical rifting criterion that is independent of the vertical temperature profile,

$$\frac{\bar{R}_{xx}^*}{\bar{R}_{xx}^{IT}} = 1. \tag{24}$$

This result from force balance can be explained intuitively. The transition from uncracked to cracked ice causes a force F_x acting on the ice through changes in gravitational potential energy U,

$$F_x = \frac{\partial U}{\partial x} = \int_{-\frac{\rho_i}{\rho_w}H}^{-\frac{\rho_i}{\rho_w}H + d_b} (\rho_w - \rho_i) g z \mathrm{d}z - \int_{\left(1-\frac{\rho_i}{\rho_w}\right)H}^{\left(1-\frac{\rho_i}{\rho_w}\right)H - d_s} \rho_i g z \mathrm{d}z. \tag{25}$$

https://doi.org/10.1017/jog.2024.52 Published online by Cambridge University Press

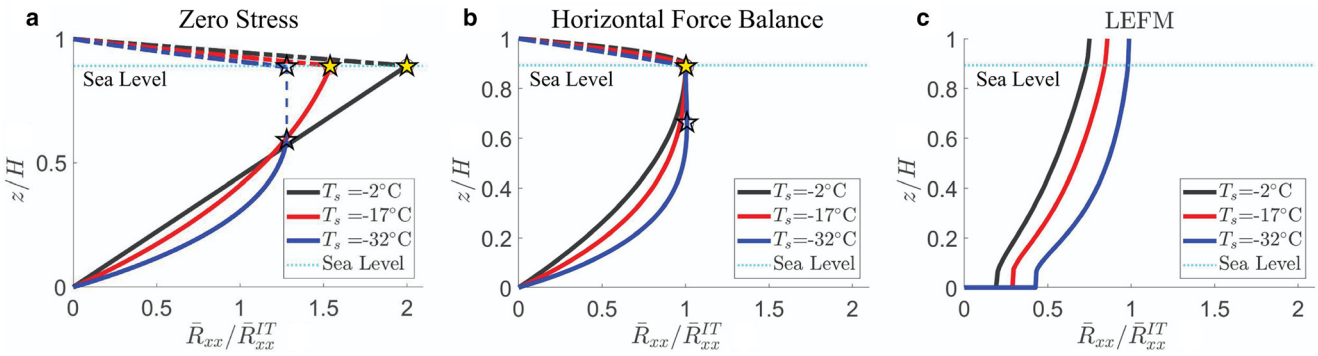

Figure 4. Predicted crevasse depths normalized by ice thickness H for (a) the Zero Stress approximation, (b) Horizontal Force Balance and (c) Linear Elastic Fracture Mechanics given a linear temperature profile in the vertical direction from a basal temperature of −2 °C to surface temperature T_s. The y-axes are non-dimensional height from the ice shelf base, and the x-axes are depth-averaged resistive stress normalized by depth-averaged ice tongue resistive stress. The solid lines are the normalized height of basal crack tips measured from the base upwards, and the dash-dotted lines are the normalized height of surface crevasse tips measured from the surface downwards. Rifting is represented by yellow stars where basal and surface crevasses meet at sea level and by open stars for unstable basal crack depth d_b^* (e.g. Eqn (5)), respectively. For LEFM, rifting occurs when the basal crack, without the presence of a surface crack, fully penetrates the ice thickness. The isothermal cases presented here at $T = -2$ °C of the Zero Stress approximation and Horizontal Force Balance are analytical, while all other results are numerical.

The terms on the right-hand side represent the changes in force due to water replacing ice and ice replaced by a free surface for basal and surface crevasse opening, respectively. We reset $z = 0$ to sea level to highlight the similarity to the compressive buckling problem in equation (B5) of Coffey and others (2022). In the case of rifting with cracks meeting at sea level, this force is

$$F_x = -\frac{1}{2}\left(1 - \frac{\rho_i}{\rho_w}\right)\rho_i g H^2 = -H\bar{R}^*_{xx}. \tag{26}$$

To uphold static HFB $\Sigma F_x = 0$, we see that the tensile force in the ice must be the negative of this value. Thus, the resistive stress required for rifting is that of a 1D ice tongue, as in Eqn (24).

2.4. Comparison between the three fracture models

The comparison between the three fracture models is presented in Figure 4. In order of smallest to largest rifting threshold $\bar{R}^*_{xx}/\bar{R}^{IT}_{xx}$, or highest to lowest vulnerability to rifting, we have LEFM, HFB and the Zero Stress approximation for all temperatures analyzed in this study. We note that the influence of temperature is distinct between the three theories; while HFB has negligible temperature dependence, colder surface temperatures lower the rifting threshold $\bar{R}^*_{xx}/\bar{R}^{IT}_{xx}$ for the Zero Stress approximation yet increase the rifting threshold for LEFM. However, for HFB in Figure 4b, colder surface temperatures cause a decrease (increase) in basal (surface) crevasse depth, yet leave the rifting threshold stress unchanged. In summary, the rifting stress ratios that account for a vertically varying temperature profile for each theory and the formula we use to compute the dimensionless stress from ice shelf data are:

$$\text{Zero Stress}: \quad \frac{\bar{R}^*_{xx}}{\bar{R}^{IT}_{xx}} = 2\frac{\rho_w}{\rho_i}\frac{d_b^*}{H}\frac{\overline{\tilde{B}(T)}}{\tilde{B}\left(T\left(d_b^*/H\right)\right)}$$

$$\text{LEFM}: \text{Analytical approximation (1\%-5\%):}$$

$$\frac{\bar{R}^*_{xx}}{\bar{R}^{IT}_{xx}} = \frac{\frac{2}{3}\left(2 - \frac{\rho_i}{\rho_w}\right)}{2\tilde{z}_0\left(1 - \left(\tilde{z}_0\left(\exp\left(\frac{1}{\tilde{z}_0}\right) - 1\right)\right)^{-1}\right)}$$

$$\text{HFB}: \frac{\bar{R}^*_{xx}}{\bar{R}^{IT}_{xx}} = 1$$

$$\text{Data}: \frac{\bar{R}_{xx}}{\bar{R}^{IT}_{xx}} = \frac{2\bar{B}\dot{\bar{\epsilon}}^{1/n}_{xx}}{\frac{1}{2}\left(1 - \frac{\rho_i}{\rho_w}\right)\rho_i g H}.$$

Note that when we compute the dimensionless stress with ice shelf data, we first confirm in Figure 8 that regions are approximately 1D to uphold the plane strain assumption of LEFM, and estimate the stress state prior to rifting through estimating the unbroken ice thickness as discussed in detail in Appendix A.

We can understand the temperature effects on crack depth and rifting stress through intuitive explanations of each theory, with extended discussions in Appendices C through E. One way to understand the temperature effects is decomposing the depth-varying resistive stress into a depth-averaged component and a vertically varying component, $R_{xx}(z) = \bar{R}_{xx} + R'_{xx}(z)$. Figure 12 shows that $R'_{xx}(z)$ is negative toward the ice base and positive toward the ice surface. The Zero Stress approximation is determined by the net longitudinal stress σ_n in Eqn (1) at the crack tip; thus, due to the sign of $R'_{xx}(z)$, we see smaller basal crack depths toward the base and smaller depth-averaged rifting stress thresholds $\bar{R}^*_{xx}$ for colder T_s in Figure 4a. In contrast, numerical LEFM results in Figure 4c show smaller crack depths and larger depth-averaged rifting stress thresholds $\bar{R}^*_{xx}$ for colder ice. The analytical explanation is provided in the LEFM section and Appendix D. Finally, our HFB theory inherits the assumption of local force balance at crack tips from the Zero Stress theory, yielding smaller basal (larger surface) stable crack depths for colder T_s with larger vertically varying resistive stress $R_{xx}(z)$ as shown in Figure 4b. The rifting stress threshold mostly results from stable basal and surface crevasse depths meeting at sea level. The effects of temperature on the ratio of the surface to basal crack depth (19) vanish as the surface and basal cracks approach sea-level, as seen in Figure 4b. Thus, the rifting stress threshold in HFB is well-approximated by the isothermal result of $\bar{R}^*_{xx}/\bar{R}^{IT}_{xx} = 1$. Overall, the effect of temperature on basal crevasse depth and rift initiation depends strongly on the chosen theory.

2.5. Robin temperature profile

To check the sensitivity of our conclusions to temperature profiles that are not linear, we run through the analyses of this paper assuming a Robin temperature profile (Robin, 1955). While this solution is strictly valid for an ice divide, the curvature of the profile is closer to observed temperature from borehole data in some cases than a linear temperature profile (Thomas and MacAyeal, 1982; Rist and others, 2002; Craven and others, 2009; Sergienko and others, 2013; Tyler and others, 2013). The goal of this exercise is not to create highly realistic temperature profiles by modeling the computationally expensive temperature evolution and advection from ice divides to ice shelves, but is instead meant as a

https://doi.org/10.1017/jog.2024.52 Published online by Cambridge University Press

sensitivity test of the results to the assumed temperature profile. As with the example plotted in Figure 5, the Robin family of temperature profiles take the form

$$T(\tilde{z}) = T_s + \frac{q}{k}\sqrt{\frac{\pi\kappa H_d}{2\dot{a}}}\left[\mathrm{erf}\left(\sqrt{\frac{\dot{a}H_d}{2\kappa}}\right) - \mathrm{erf}\left(\tilde{z}\sqrt{\frac{\dot{a}H_d}{2\kappa}}\right)\right], \quad (27)$$

with surface temperature T_s, thermal diffusivity $\kappa \equiv k/(\rho_i c_p) \approx 10^{-6}$ $m^2\ s^{-1}$ defined by thermal conductivity to ice density and specific heat of ice, rescaled vertical coordinate $\tilde{z} = z/H$ with value 0 at the ice base and 1 at the surface, basal heat flux q, ice divide thickness $H_d \approx 1000$ m and snowfall rate $\dot{a} \approx 0.1$ m a^{-1} based on Fowler and Ng (2020). We note that the ice divide thickness H_d is set to match the Sandhäger and others (2005) profile at sea level, as demonstrated in Figure 5. We match the temperature profiles near sea level, as this region is important in determining if basal crevasses propagate to form rifts. Considering the ice-ocean temperature at the bottom of ice shelf $T_b = -2$ °C, we have

$$T_b = T_s + \frac{q}{k}\sqrt{\frac{\pi\kappa H_d}{2\dot{a}}}\mathrm{erf}\left(\sqrt{\frac{\dot{a}H_d}{2\kappa}}\right), \quad (28)$$

Substituting (28) into (27) gives a simple form of the Robin profile,

$$T(\tilde{z}) = T_s + (T_b - T_s)\left(1 - \frac{\mathrm{erf}\left(\tilde{z}\sqrt{\frac{\dot{a}H_d}{2\kappa}}\right)}{\mathrm{erf}\left(\sqrt{\frac{\dot{a}H_d}{2\kappa}}\right)}\right). \quad (29)$$

The remainder of the Robin profile analyses for each fracture theory is carried out the same way as presented in the body of this paper. In the next section, we show that the rifting stress thresholds are not significantly impacted by using a Robin temperature profile versus linear temperature profile.

3. Comparison with observations

As the three fracture theories predict distinct critical stresses that drive the basal crevasse to rift transition, we evaluate the applicability of each theory by comparison with observed rift locations. We analyze our results in two ways. First, we plot the predicted rift locations on MODIS MOA (Scambos and others, 2007; Haran and others, 2018) compared with the rifts previously mapped by Walker and others (2013), labeled as 'true rifts' and colored in blue on Ross Ice Shelf (RIS) in Figure 6. The goal of these rift formation theories is to maximize the overlap between the predicted and true rifts, colored in green in Figure 6.

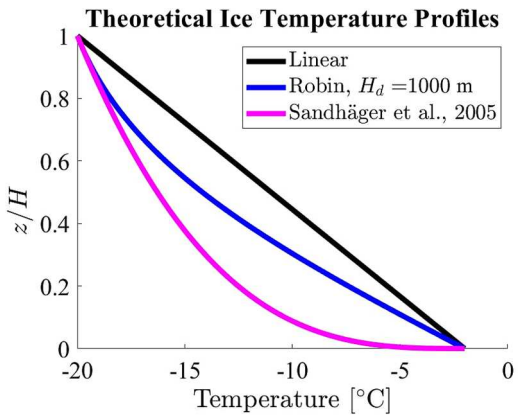

Figure 5. Theoretical ice shelf temperature profiles.

Because we do not have values of strain rate or surface temperature at the time of rifting, the estimated stress state (Fig. 6e) uses modern surface temperature (van Wessem and others, 2018) and strain rate (Wearing, 2017) values, with limitations discussed in Appendix A. In Figure 6, we see that on the RIS rifts identified by Walker and others (2013), Zero Stress with a vertical temperature profile (Fig. 6b) underpredicts known rifts as shaded in blue. Similarly, LEFM with a depth-averaged resistive stress $\bar{R}_{xx}$ (Fig. 6c), with analytical result given by Zarrinderakht and others (2022), overpredicts rifts into areas they were not observed as shaded in red. LEFM with a vertical temperature profile (Fig. 6a) and HFB (Fig. 6d) are the most accurate theories for these RIS rifts. Their differences are small enough to warrant more observations to distinguish which theory is most applicable.

Second, we construct a crack stability plot of the critical stress $\bar{R}^*_{xx}/\bar{R}^{IT}_{xx}$ for rift formation for each theory as a function of the ice surface temperature T_s, as shown by the curves in Figure 7. Noticeably, surface temperature has a negligible effect on the rifting threshold for the HFB; the rifting stress is that of a freely floating ice tongue, $\bar{R}^*_{xx} = \bar{R}^{IT}_{xx} \equiv (1 - \rho_i/\rho_w)\rho_i g H/2$ (light blue line in Fig. 7). Comparing the rift formation stress criteria, the depth-averaged Zero Stress approximation (dashed blue line) requires a resistive stress 200% of that of a freely floating ice tongue to cause rifts, while the isothermal LEFM theory as presented by Zarrinderakht and others (2022) (dashed magenta line) requires only 74% of that of a freely floating ice tongue to initiate rifts. It is our goal to constrain this substantial uncertainty in the rift initiation stress threshold of these two theories, presented by the dashed lines of Figure 7.

We quantitatively compare the rift criteria with the observed rifts on the RIS in Figure 6 and Larsen C Ice Shelf (LCIS) in Figure 10. We identify the extensional, 1D flow regions excluding the high-strain-rate rift locations on the RIS and LCIS in Figure 11, and plot the mean depth-averaged resistive stress and surface temperature across these regions in orange symbols in Figure 7 with one standard deviation of uncertainty due to the variation of resistive stress and surface temperature across these regions. The bulk of the non-rift ice shelf data should lie below the curves in Figure 7. While LEFM with depth-averaged resistive stress may look accurate in Figure 7, the overprediction in red is clear in Figures 6c and 10c. Additionally, the lack of force balance from isothermal Zero Stress (dashed blue line) and Zero Stress with vertical temperature variation (solid green line) invalidates these predictions on theoretical grounds. This lack of force balance manifests as an underprediction of rifting, as discussed in Appendix A and demonstrated in Figure 16. Therefore, within the uncertainty of our data as discussed in the Uncertainties of the data-model comparison subsection and Appendix F, our results on two ice shelves suggest LEFM and HFB considering the vertically varying ice temperatures are the most accurate theories for predicting the rift locations on the RIS and LCIS.

Figures 14, 15, 16 and 17 show that the conclusions drawn from the linear profile are also applicable to the Robin temperature profile. The rift formation stress curves with linear and Robin temperature profiles in Figure 16 are similar. The relative accuracy of each theory in Figures 14 and 15 is comparable to Figures 6 and 10, respectively. Overall, the conclusions of the paper with a linear temperature profile are unchanged given our estimate of a Robin temperature profile.

4. Discussion and conclusions

4.1. Threshold stress for the transition from basal crevasses to rifts

In this paper, we have determined several rift formation stress criteria as functions of surface temperature for linear temperature

https://doi.org/10.1017/jog.2024.52 Published online by Cambridge University Press

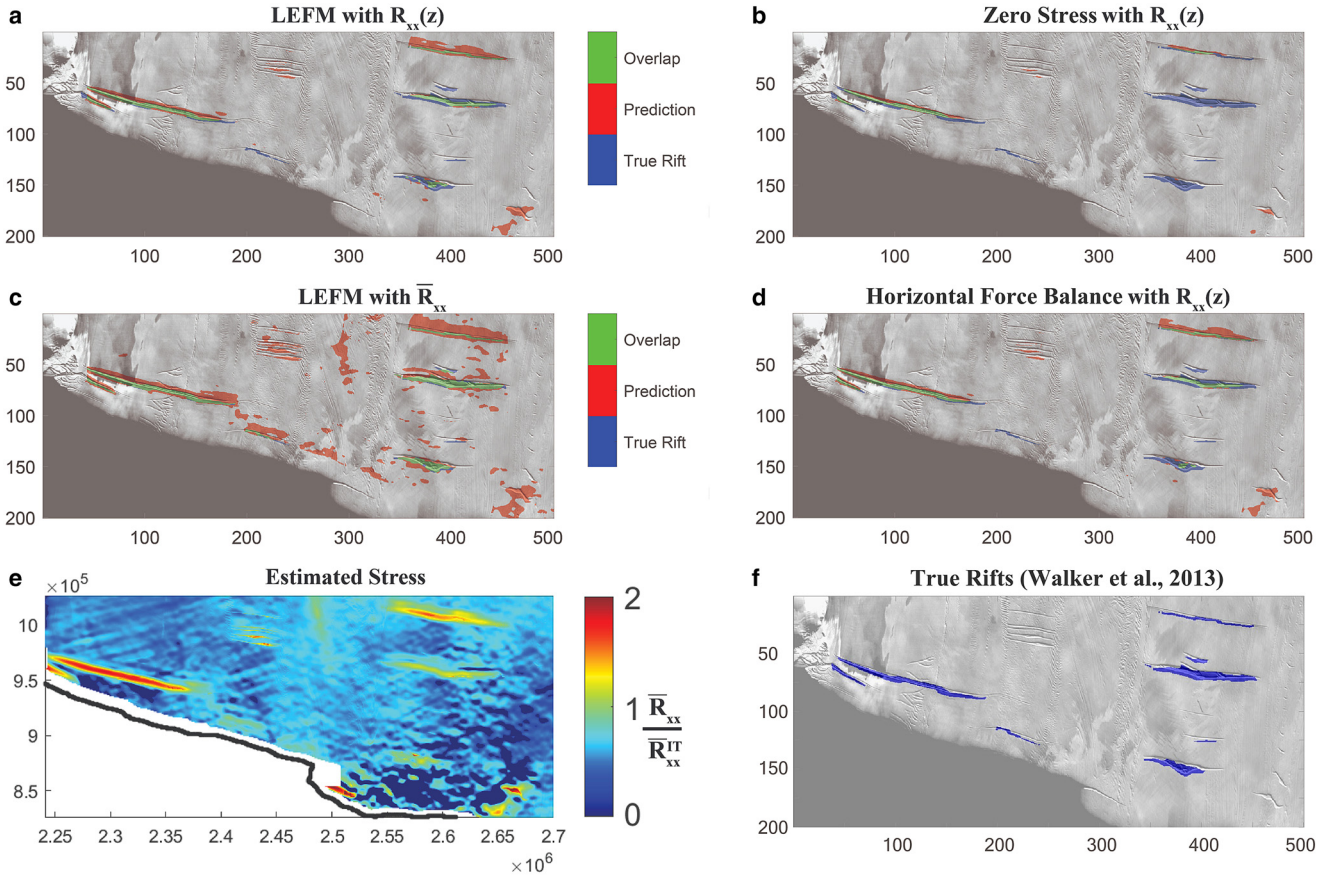

Figure 6. Figures (a) to (d) are map views in kilometers of observed (marked in blue) and theoretically predicted rifts (marked in red) on the Ross Ice Shelf, overlain on MODIS MOA 2014 (Haran and others, 2018; Scambos and others, 2007), with correctly predicted rifts in green. Rift formation theories are (a) LEFM with depth-varying stress due to temperature variation $R_{xx}(z)$, (b) Zero Stress with $R_{xx}(z)$, (c) LEFM with depth-averaged stress $\bar{R}_{xx}$ and (d) Horizontal Force Balance with $R_{xx}(z)$. Figure (e) is the estimated resistive stress ratio used for panel (a–d) with axes in meters. (f) Observed rifts were identified by Walker and others (2013) and shown in blue.

profiles. We then use remote-sensing and model output data to determine which theory best predicts observed rifts. We find that Zero Stress with either depth-averaged or vertically varying resistive stress underpredicts rifts, due in part to the inconsistency that the formulations do not uphold force balance in a control volume. On the other hand, we find that LEFM with depth-averaged resistive stress overpredicts rifts. Our result shows that on the RIS and LCIS, HFB and LEFM with vertically varying resistive stress are the most accurate theories for correctly predicting rifts and non-rifts. Further distinction between these two theories is inhibited by the number of rifts and uncertainty of current data products used in this study. However, given that buoyancy is expected to stabilize deep basal crevasses (Logan and others, 2013; Zarrinderakht and others, 2022) and is not available analytically for the LEFM models, we expect the rift initiation stress threshold of LEFM models to increase. Thus, for the initialization of rifts in ice-sheet models, we recommend using the simple, analytical, physically consistent theory of HFB, with rift initiation threshold $\bar{R}^*_{xx}/\bar{R}^{IT}_{xx} = 1$ (Eqn (24)). This rifting threshold has been numerically predicted for an isolated basal crevasse

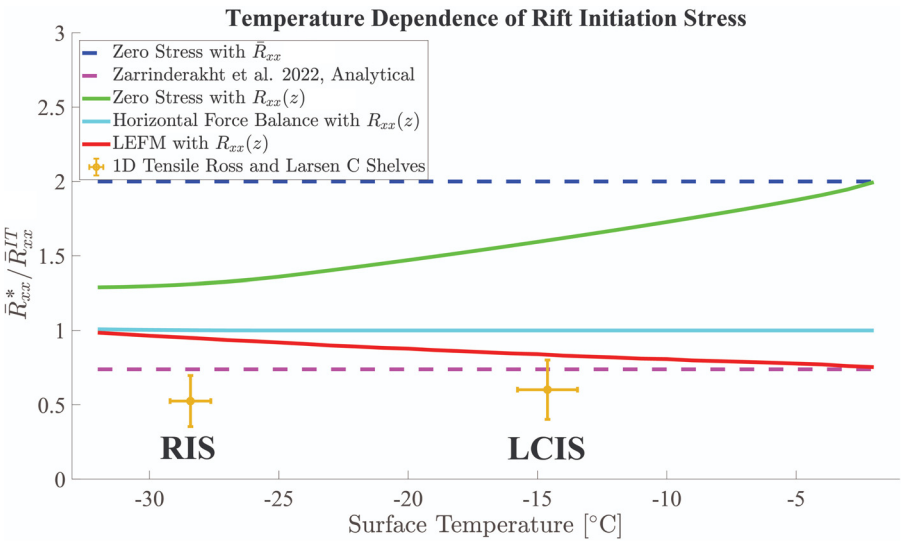

Figure 7. Non-dimensional resistive stress required to initiate rifts versus surface temperature, assuming a linear temperature profile. The solid lines account for vertically varying temperature structure through depth-varying stress $R_{xx}(z)$, whereas the dashed lines use depth-averaged resistive stress $\bar{R}_{xx}$. For a given theory, the regions above and below the curve are predicted as a rift and non-rift, respectively. Ice shelf stresses averaged over regions that are not rifted and obey the 1D fracture assumptions are plotted in orange symbols with mean and standard deviation. These data are shown in map view in Figure 11. We use the average thickness in the non-rift area as H to calculate $\bar{R}^{IT}_{xx}$. In this figure, surface temperatures colder than −25 °C are on the Ross Ice Shelf (RIS), whereas those warmer are on the Larsen C Ice Shelf (LCIS). While the Zarrinderakht and others (2022) line in dashed magenta looks compelling with the intact ice shelf data in orange, map view analyses (see Figs 6c, 10c) show that it overpredicts rifts.

https://doi.org/10.1017/jog.2024.52 Published online by Cambridge University Press

(Buck, 2023). Further, this study validates this result against observed rifts on RIS and LCIS. In the Robin temperature profile subsection, we compared the results between linear and Robin temperature profiles (Robin, 1955), both showing a negligible temperature dependence of this rifting threshold.

4.2. Stability of ice tongues

A question may then naturally arise: How can the freely floating ice tongue stress be sufficient to form rifts, yet we see ice tongues exist in nature? It is important here to draw a distinction between idealized 1D, constant thickness, zero yield-strength ice tongues and those found in nature: any perturbations to the stress field, mass balance, spatially varying thickness and crack geometry can influence the stability of real ice tongues. For example, sea ice or ice mélange can stabilize these structures through potentially providing a force buttressing the ice shelf and dampening ocean waves that would otherwise induce ice shelf flexural stress (Vaughan, 1995; Bromirski and others, 2010; Sergienko, 2010, 2013; Hulbe and others, 2016; Massom and others, 2018; Miles and others, 2020; Gomez-Fell and others, 2022), with recent work arguing this idea may be most applicable for thin ice (Bassis and others, 2024). Recent observational work analyzing the Eastern Antarctic Peninsula found that 94% of ice shelf calving occurred during or shortly after the removal of sea ice (Christie and others, 2022), highlighting the importance of external atmospheric and oceanic conditions. The stress threshold and environmental sensitivity of ice tongue calving is crucial for predicting calving and potential subsequent changes in dense water formation, carbon export and biological productivity, as evidenced by the 2010 Mertz Glacier Tongue calving (Kusahara and others, 2011; Shadwick and others, 2013; Ohshima and others, 2016).

4.3. Model limitations

This idealized study is subject to several limitations. We assume 2D (x, z), incompressible, homogeneous density, elastic modulus and fracture toughness (Rist and others, 2002) ice shelves with zero across-flow strain rate and zero shear strain rate. These theories do not include local thickness variation, creep closure, sub- and super-buoyant flexure (Benn and others, 2017), ice front bending stresses (Reeh, 1968), grain size dependence of yield stress (Ranganathan and others, 2021), crack tip shielding (Clayton and others, 2022), snow accumulation, basal melting (Bassis and Ma, 2015; Kachuck and others, 2022; Buck, 2023) and marine ice accumulation. While we take a constant density, we note recent work that suggests the importance of vertical density variation for surface crevasses (Gao and others, 2023).

To be consistent with the plane strain assumptions of our fracture theories when comparing with observations, we develop a strain rate criterion in Appendix A to validate locations where the flow is approximately 1D and Mode I fracture is applicable. In reality, ice shelves can also have their stress states altered due to 3D effects such as shear fractures (van der Veen, 1999) and torque from ocean currents (Gomez-Fell and others, 2022; Huth and others, 2022). The interactions of the ocean, sea ice, mass balance, the location of additional cracks or other additional stresses may determine the stability of the ice tongues and shelves in nature by modulating the ice shelf stress. Effects such as the hydrographic conditions in basal crevasses, crevasse-, tidal- or tsunami-induced flexural stresses (Walker and others, 2013; Brunt and others, 2011; Bromirski and others, 2017; Gerstoft and others, 2017), viscous creep closure, fatigue failure (Zehnder, 2012), potentially non-negligible process zones (Zehnder, 2012), realistic ice rheology or the time-dependent evolution (Lawn, 1993) of basal crevasses evolving into rifts are neglected. We leave the coupling of these processes to future work.

One inherent source of model uncertainty is the formation mechanism of the rifts on RIS and LCIS that we analyze in this study. As mentioned in the introduction, we can not definitively claim that the rifts were created by basal crevasse propagation. Surface crevasse hydrofracture is a relatively well-studied problem, and ample surface meltwater can form a rift on an ice shelf (Weertman, 1973, 1974; van der Veen, 1998b; Banwell and others, 2013; Duddu and others, 2020; Lai and others, 2020). However, seawater-filled a basal crevasses are predicted to be roughly nine times deeper than dry surface crevasses across several isothermal crevasse theories (Nye, 1955; Nick and others, 2010; Weertman, 1973; van der Veen, 1998b,1998a). This implies that in the absence of strong surface melt (Morris and Vaughan, 2003; van Wessem and others, 2023) basal crevasse is the likely rift formation mechanism.

4.4. Uncertainties of the data-model comparison

Both data products and ice rheology contribute sources of uncertainty to this study. We discuss uncertainty in data products in Appendix F, where we estimate an upper bound in uncertainty and see that the largest source of uncertainty is in the estimation of ice thickness on the Ross Ice Shelf (Morlighem and others, 2020). Another source of uncertainty comes from the ice rheology. We note that there is uncertainty in the flow law exponent n (Goldsby and Kohlstedt, 2001; Qi and others, 2017; Bons and others, 2018; Millstein and others, 2022) and therefore in the parameters of Eqns (2) and (4) (Zeitz and others, 2020). This will affect both our estimation of stress as shown in Figure 6e, and the rift initiation stress threshold curves in Figures 7, 16 for Zero Stress and LEFM. However, one great benefit of the HFB model is an insensitivity to rheology in the limit of rifting. This is exemplified in Figure 4b: while crack depths are different for different surface temperatures, the rift initiation threshold is approximately the same across various vertical temperature profiles. Furthermore, as demonstrated in the Robin temperature profile subsection the rift initiation stress threshold between linear and Robin temperature profiles is the same (see Figs 7, 16). Additionally, as HFB best matches observations (see Figs 6, 10), the leading rift initiation theory of this study demonstrates a unique resilience to rheological uncertainty.

4.5. Future applications

Areas of future research that may build on this study are at least threefold: (1) initializing rifts with the HFB model in numerical ice sheet/shelf models, (2) analyzing the impacts of fracture model on processes governing the ice shelf stability; HFB predicts much deeper crack depths than the Zero Stress approximation and (3) incorporating higher temporal-resolution observations to observationally constrain the rifting stress threshold.

First, this study provides a simple analytical rift formation stress threshold and crack depths that can be coupled with numerical ice-sheet simulations. Damage mechanics has shown great promise (Huth and others, 2021), capturing the path of rift propagation to form iceberg A68 from Larsen C (Huth and others, 2023). However, this model requires the specification of a starter rift (in this case near the Gipps Ice Rise) to predict its horizontal propagation. Coupling rift propagation models with our HFB theory for rift initialization, $\bar{R}^{*}_{xx}/\bar{R}^{IT}_{xx} = 1$ can potentially advance simulations' ability to model rifts from initiation to iceberg detachment.

Second, another interesting extension would be embedding HFB into the analysis of processes that require analytical fracture

https://doi.org/10.1017/jog.2024.52 Published online by Cambridge University Press

theory, such as Bassis and Walker (2012); Pollard and others (2015); Bassis and Ma (2015). For example, because the HFB model predicts much deeper cracks compared with the Zero Stress approximation that was used in Pollard and others (2015), implementing our HFB fracture model instead could yield substantially different outcomes, making ice shelves more vulnerable to fracture than predicted by Pollard and others (2015).

Third, future work monitoring the rift initiation process with high temporal resolution can provide stronger constraints on the rifting stress threshold. As shown in Figure 1c and discussed in Appendix B, the best estimates of stress in this study rely on monthly averaged strain rate data. However, the speed of horizontal rift propagation can be much faster than what can be observed from satellite imagery (Olinger and others, 2024). While it is promising that we see a clear increase in surface strain rate and thus stress estimates in Figure 1c, it is clear that higher temporal-resolution measurements of strain rate, cross-rift altimetry and/or field-based data of the basal crevasse to rift transition would help to constrain these rifting stress threshold theories.

This study advances the common fracture theories used in glaciology through the incorporation of vertical stress variations due to the temperature dependence of the ice hardness, and the HFB model that properly accounts for HFB. The different rifting stress theories coupled with ice shelf simulations could lead to distinct calving predictions. Importantly, the Zero Stress approximation would largely under-predict the crevasse depths and stability compared with the HFB model, and underestimate the mass loss of ice shelves over the coming centuries.

Acknowledgements. We acknowledge funding from NSF's Office of Polar Programs through OPP-2235051. C.-Y.L. acknowledges NASA for partial support via Cryosphere Award 80NSSC21K1003.

References

Banwell AF, MacAyeal DR and Sergienko OV (2013) Breakup of the Larsen B ice shelf triggered by chain reaction drainage of supraglacial lakes. *Geophysical Research Letters* **40**(22), 5872–5876. doi: 10.1002/2013GL057694

Bassis J and Ma Y (2015) Evolution of basal crevasses links ice shelf stability to ocean forcing. *Earth and Planetary Science Letters* **409**, 203–211. doi: 10.1016/j.epsl.2014.11.003

Bassis JN and Kachuck SB (2023) Beyond the stokes approximation: shallow visco-elastic ice-sheet models. *Journal of Glaciology* 1–12. doi: 10.1017/jog.2023.75

Bassis JN and Walker CC (2012) Upper and lower limits on the stability of calving glaciers from the yield strength envelope of ice. *Proceedings of the Royal Society A: Mathematical, Physical and Engineering Sciences* **468**(2140), 913–931. doi: 10.1098/rspa.2011.0422

Bassis JN and 9 others (2024) Stability of ice shelves and ice cliffs in a changing climate. *Annual Review of Earth and Planetary Sciences* **52**, 221–247. doi: 10.1146/annurev-earth-040522-122817

Benn DI, Hulton NRJ and Mottram RH (2007) 'Calving laws', 'sliding laws' and the stability of tidewater glaciers. *Annals of Glaciology* **46**, 123–130. doi: 10.3189/172756407782871161

Benn DI and 7 others (2017) Melt-under-cutting and buoyancy-driven calving from tidewater glaciers: new insights from discrete element and continuum model simulations. *Journal of Glaciology* **63**(240), 691–702. doi: 10.1017/jog.2017.41

Bons PD and 6 others (2018) Greenland ice sheet: higher nonlinearity of ice flow significantly reduces estimated basal motion. *Geophysical Research Letters* **45**(13), 6542–6548. doi: 10.1029/2018GL078356

Borstad CP and 6 others (2012) A damage mechanics assessment of the Larsen B ice shelf prior to collapse: toward a physically-based calving law. *Geophysical Research Letters* **39**(18), L18502. doi: 10.1029/2012GL053317

Bromirski PD, Sergienko OV and MacAyeal DR (2010) Transoceanic infragravity waves impacting Antarctic ice shelves. *Geophysical Research Letters* **37**(2), L02502. doi: 10.1029/2009GL041488

Bromirski PD and 8 others (2017) Tsunami and infragravity waves impacting Antarctic ice shelves. *Journal of Geophysical Research: Oceans* **122**(7), 5786–5801. doi: 10.1002/2017JC012913

Brunt KM, Okal EA and MacAyeal DR (2011) Antarctic ice-shelf calving triggered by the Honshu (Japan) earthquake and tsunami, March 2011. *Journal of Glaciology* **57**(205), 785–788. doi: 10.3189/002214311798043681

Buck WR (2023) The role of fresh water in driving ice shelf crevassing, rifting and calving. *Earth and Planetary Science Letters* **624**, 118444. doi: 10.1016/j.epsl.2023.118444

Buck WR (2024) The effect of ice rheology on shelf edge bending. *EGUsphere* **2024**, 1–17.

Buck WR and Lai CY (2021) Flexural control of basal crevasse opening under ice shelves. *Geophysical Research Letters* **48**(8), e2021GL093110. doi: 10.1029/2021GL093110.

Chartrand R (2017) Numerical differentiation of noisy, nonsmooth, multidimensional data. In *2017 IEEE Global Conference on Signal and Information Processing (GlobalSIP)*, pp. 244–248.

Child SF, Stearns LA, van der Veen CJ and Elósegui P (2021) Basal crevasse formation on Byrd glacier, East Antarctica, as proxy for past subglacial flooding events. *Geophysical Research Letters* **48**(15), e2020GL090978. doi: 10.1029/2020GL090978

Christie FD and 5 others (2022) Antarctic ice-shelf advance driven by anomalous atmospheric and sea-ice circulation. *Nature Geoscience* **15**(5), 356–362.

Clayton T, Duddu R, Siegert M and Martínez-Pañeda E (2022) A stress-based poro-damage phase field model for hydrofracturing of creeping glaciers and ice shelves. *Engineering Fracture Mechanics* **272**, 108693. doi: 10.1016/j.engfracmech.2022.108693

Coffey NB and 6 others (2022) Enigmatic surface rolls of the Ellesmere ice shelf. *Journal of Glaciology* **68**(271), 867–878. doi: 10.1017/jog.2022.3

Colgan W and 6 others (2016) Glacier crevasses: observations, models, and mass balance implications. *Reviews of Geophysics* **54**(1), 119–161. doi: 10.1002/2015RG000504

Craven M, Allison I, Fricker HA and Warner R (2009) Properties of a marine ice layer under the Amery ice shelf, East Antarctica. *Journal of Glaciology* **55**(192), 717–728. doi: 10.3189/002214309789470941

Cuffey KM and Paterson WSB (2010) *The Physics of Glaciers*, 4th edn. Amsterdam: Academic Press.

De Robin GQ (1974) Depth of water-filled crevasses that are closely spaced. *Journal of Glaciology* **13**(69), 543–543. doi: 10.3189/S0022143000023285

Duddu R, Jiménez S and Bassis J (2020) A non-local continuum poro-damage mechanics model for hydrofracturing of surface crevasses in grounded glaciers. *Journal of Glaciology* **66**(257), 415–429. doi: 10.1017/jog.2020.16

Dupont TK and Alley RB (2005) Assessment of the importance of ice-shelf buttressing to ice-sheet flow. *Geophysical Research Letters* **32**(4), L04503. doi: 10.1029/2004GL022024

Fowler A and Ng F (2020) *Glaciers and Ice Sheets in the Climate System: The Karthaus Summer School Lecture Notes*. Switzerland: Springer Nature.

Freed-Brown J, Amundson JM, MacAyeal DR and Zhang WW (2012) Blocking a wave: frequency band gaps in ice shelves with periodic crevasses. *Annals of Glaciology* **53**(60), 85–89. doi: 10.3189/2012AoG60A120

Gao Y, Ghosh G, Jimènez S and Duddu R (2023) A finite-element-based cohesive zone model of water-filled surface crevasse propagation in floating ice tongues. *Computing in Science & Engineering* **25**(3), 8–16. doi: 10.1109/MCSE.2023.3315661

Gerstoft P and 6 others (2017) Tsunami excitation of the Ross ice shelf, Antarctica. *The Journal of the Acoustical Society of America* **141**, 3526–3526. doi: 10.1121/1.4987434

Glen J (1958) The flow law of ice: a discussion of the assumptions made in glacier theory, their experimental foundations and consequences. *IASH Publication* **47**(171), e183.

Goelzer H and 41 others (2020) The future sea-level contribution of the Greenland ice sheet: a multi-model ensemble study of ISMIP6. *The Cryosphere* **14**(9), 3071–3096. doi: 10.5194/tc-14-3071-2020

Goldsby DL and Kohlstedt DL (2001) Superplastic deformation of ice: experimental observations. *Journal of Geophysical Research: Solid Earth* **106**(B6), 11017–11030. doi: 10.1029/2000JB900336

Gomez-Fell R, Rack W, Purdie H and Marsh O (2022) Parker ice tongue collapse, Antarctica, triggered by loss of stabilizing land-fast sea ice.

Geophysical Research Letters **49**(1), 1–11, e2021GL096156. doi: 10.1029/2021GL096156.

Haran T, Bohlander J, Scambos T, Painter T and Fahnestock M (2013) 2005, updated 2013. MODIS Mosaic of Antarctica 2003-2004 (moa2004) image map, version 1. moa125_r1_hp1.img.gz. Boulder, Colorado USA. NASA National Snow and Ice Data Center Distributed Active Archive Center. doi: 10.7265/N5ZK5DM5. Accessed 14/06/2021.

Haran T and 5 others (2018) Measures MODIS Mosaic of Antarctica 2013-2014 (moa2014) image map, version 1. doi: 10.5067/RNF17BP824UM

Haseloff M and Sergienko OV (2018) The effect of buttressing on grounding line dynamics. *Journal of Glaciology* **64**(245), 417–431. doi: 10.1017/jog.2018.30

Hulbe CL, Rignot E and Macayeal DR (1998) Comparison of ice-shelf creep flow simulations with ice-front motion of Filchner-Ronne ice shelf, Antarctica, detected by SAR interferometry. *Annals of Glaciology* **27**, 182–186. doi: 10.3189/1998AoG27-1-182-186

Hulbe CL and 5 others (2016) Tidal bending and strand cracks at the Kamb Ice Stream grounding line, West Antarctica. *Journal of Glaciology* **62**(235), 816–824. doi: 10.1017/jog.2016.74

Huth A, Duddu R and Smith B (2021) A generalized interpolation material point method for shallow ice shelves. 2: Anisotropic nonlocal damage mechanics and rift propagation. *Journal of Advances in Modeling Earth Systems* **13**(8), e2020MS002292. doi: 10.1029/2020MS002292

Huth A, Adcroft A, Sergienko O and Khan N (2022) Ocean currents break up a tabular iceberg. *Science Advances* **8**(42), eabq6974 doi: 10.1126/sciadv.abq6974

Huth A, Duddu R, Smith B and Sergienko O (2023) Simulating the processes controlling ice-shelf rift paths using damage mechanics. *Journal of Glaciology* 1–14. doi: 10.1017/jog.2023.71

Jeong S, Howat IM and Bassis JN (2016) Accelerated ice shelf rifting and retreat at Pine island glacier, West Antarctica. *Geophysical Research Letters* **43**(22), 11,720–11,725. doi: 10.1002/2016GL071360

Jezek KC (1984) A modified theory of bottom crevasses used as a means for measuring the buttressing effect of ice shelves on inland ice sheets. *Journal of Geophysical Research: Solid Earth* **89**(B3), 1925–1931. doi: 10.1029/JB089iB03p01925

Jezek KC and Bentley CR (1983) Field studies of bottom crevasses in the Ross ice shelf, Antarctica. *Journal of Glaciology* **29**(101), 118–126. doi: 10.3189/S0022143000005189

Jezek KC, Bentley CR and Clough JW (1979) Electromagnetic sounding of bottom crevasses on the Ross ice shelf, Antarctica. *Journal of Glaciology* **24**(90), 321–330. doi: 10.3189/S0022143000014842

Jiménez S and Duddu R (2018) On the evaluation of the stress intensity factor in calving models using linear elastic fracture mechanics. *Journal of Glaciology* **64**(247), 759–770. doi: 10.1017/jog.2018.64

Jordan JR, Holland PR, Jenkins A, Piggott MD and Kimura S (2014) Modeling ice-ocean interaction in ice-shelf crevasses. *Journal of Geophysical Research: Oceans* **119**(2), 995–1008. doi: 10.1002/2013JC009208

Joughin I, Shapero D, Smith B, Dutrieux P and Barham M (2021) Ice-shelf retreat drives recent Pine island glacier speedup. *Science Advances* **7**(24), eabg3080. doi: 10.1126/sciadv.abg3080

Kachuck SB, Whitcomb M, Bassis JN, Martin DF and Price SF (2022) Simulating ice-shelf extent using damage mechanics. *Journal of Glaciology* **68**(271), 987–998. doi: 10.1017/jog.2022.12

Kusahara K, Hasumi H and Williams GD (2011) Impact of the Mertz glacier tongue calving on dense water formation and export. *Nature communications* **2**(1), 159.

Lai CY and 7 others (2020) Vulnerability of Antarctica's ice shelves to meltwater-driven fracture. *Nature* **584**, 574–578. doi: 10.1038/s41586-020-2627-8

Lawn B (1993) *Fracture of Brittle Solids*, 2 nd edn. Cambridge Solid State Science Series, Cambridge University Press.

Lawrence JD and 15 others (2023) Crevasse refreezing and signatures of retreat observed at Kamb Ice Stream grounding zone. *Nature Geoscience* **16**(3), 238–243. doi: 10.1038/s41561-023-01129-y

LeB Hooke R (1981) Flow law for polycrystalline ice in glaciers: comparison of theoretical predictions, laboratory data, and field measurements. *Reviews of Geophysics* **19**(4), 664–672. doi: 10.1029/RG019i004p00664

Lindstrom D and MacAyeal D (1987) Environmental constraints on West Antarctic ice-sheet formation. *Journal of Glaciology* **33**(115), 346–356. doi: 10.3189/S0022143000008947

Lipovsky BP (2020) Ice shelf rift propagation: stability, three-dimensional effects, and the role of marginal weakening. *The Cryosphere* **14**(5), 1673–1683. doi: 10.5194/tc-14-1673-2020

Litwin KL, Zygielbaum BR, Polito PJ, Sklar LS and Collins GC (2012) Influence of temperature, composition, and grain size on the tensile failure of water ice: implications for erosion on Titan. *Journal of Geophysical Research: Planets* **117**(E8), E08013. doi: 10.1029/2012JE004101

Logan L, Catania G, Lavier L and Choi E (2013) A novel method for predicting fracture in floating ice. *Journal of Glaciology* **59**(216), 750–758. doi: 10.3189/2013JoG12J210

Luckman A and 5 others (2012) Basal crevasses in Larsen C ice shelf and implications for their global abundance. *The Cryosphere* **6**, 113–123. doi: 10.5194/tc-6-113-2012

MacAyeal DR (1989) Large-scale ice flow over a viscous basal sediment: theory and application to Ice Stream B, Antarctica. *Journal of Geophysical Research: Solid Earth* **94**(B4), 4071–4087. doi: 10.1029/JB094iB04p04071

MacAyeal DR, Rignot E and Hulbe CL (1998) Ice-shelf dynamics near the front of the Filchner-Ronne ice shelf, Antarctica, revealed by SAR interferometry: model/interferogram comparison. *Journal of Glaciology* **44**(147), 419–428. doi: 10.3189/S0022143000002744

Massom RA and 5 others (2018) Antarctic ice shelf disintegration triggered by sea ice loss and ocean swell. *Nature* **558**(7710), 383–389. doi: 10.1038/s41586-018-0212-1

McGrath D and 5 others (2012a) Basal crevasses on the Larsen C ice shelf, Antarctica: implications for meltwater ponding and hydrofracture. *Geophysical Research Letters* **39**(16), L16504. doi: 10.1029/2012GL052413

McGrath D and 5 others (2012b) Basal crevasses and associated surface crevassing on the Larsen C ice shelf, Antarctica, and their role in ice-shelf instability. *Annals of Glaciology* **53**(60), 10–18. doi: 10.3189/2012AoG60A005

Miles BWJ and 5 others (2020) Intermittent structural weakening and acceleration of the Thwaites glacier tongue between 2000 and 2018. *Journal of Glaciology* **66**(257), 485–495. doi: 10.1017/jog.2020.20

Millstein JD, Minchew BM and Pegler SS (2022) Ice viscosity is more sensitive to stress than commonly assumed. *Communications Earth & Environment* **3**(1), 57.

Morlighem M (2020) Measures BedMachine Antarctica, version 2.

Morlighem M and 9 others (2020) Deep glacial troughs and stabilizing ridges unveiled beneath the margins of the Antarctic ice sheet. *Nature Geoscience* **13**(2), 132–137.

Morris EM and Vaughan DG (2003) Spatial and temporal variation of surface temperature on the Antarctic Peninsula and the limit of viability of ice shelves. *Antarctic Research Series* **79**(10), 61.1029–68.

Mouginot J, Scheuchl B and Rignot E (2012) Mapping of ice motion in Antarctica using synthetic-aperture radar data. *Remote Sensing* **4**(9), 2753–2767. doi: 10.3390/rs4092753

Mouginot J, Rignot E, Scheuchl B and Millan R (2017a) Comprehensive annual ice sheet velocity mapping using Landsat-8, Sentinel-1, and Radarsat-2 data. *Remote Sensing* **9**(4), 364. doi: 10.3390/rs9040364

Mouginot J, Scheuchl B and Rignot E (2017b) Measures Antarctic boundaries for IPY 2007–2009 from satellite radar, version 2. Boulder, Colorado USA. NASA National Snow and Ice Data Center Distributed Active Archive Center. doi: 10.5067/AXE4121732AD. Accessed 10/07/2023.

Murray T and 9 others (2015) Dynamics of glacier calving at the ungrounded margin of Helheim glacier, Southeast Greenland. *Journal of Geophysical Research: Earth Surface* **120**(6), 964–982. doi: 10.1002/2015JF003531

Nicholls KW and 5 others (2015) A ground-based radar for measuring vertical strain rates and time-varying basal melt rates in ice sheets and shelves. *Journal of Glaciology* **61**(230), 1079–1087. doi: 10.3189/2015JoG15J073

Nick F, Van Der Veen C, Vieli A and Benn D (2010) A physically based calving model applied to marine outlet glaciers and implications for the glacier dynamics. *Journal of Glaciology* **56**(199), 781–794. doi: 10.3189/002214310794457344

Nye JF (1955) Comments on Dr. Loewe's letter and notes on crevasses. *Journal of Glaciology* **2**(17), 512–514. doi: 10.3189/S0022143000032652

Ohshima KI, Nihashi S and Iwamoto K (2016) Global view of sea-ice production in polynyas and its linkage to dense/bottom water formation. *Geoscience Letters* **3**, 1–14.

Olinger SD, Lipovsky BP and Denolle MA (2024) Ocean coupling limits rupture velocity of fastest observed ice shelf rift propagation event. *AGU Advances* **5**(1), e2023AV001023. doi: 10.1029/2023AV001023

https://doi.org/10.1017/jog.2024.52 Published online by Cambridge University Press

Pollard D, DeConto RM and Alley RB (2015) Potential Antarctic ice sheet retreat driven by hydrofracturing and ice cliff failure. *Earth and Planetary Science Letters* **412**, 112–121.
Pralong A and Funk M (2005) Dynamic damage model of crevasse opening and application to glacier calving. *Journal of Geophysical Research: Solid Earth* **110**(B1), B01309. doi: 10.1029/2004JB003104
Pritchard H and 5 others (2012) Antarctic ice loss driven by ice-shelf melt. *Nature* **484**, 502–505.
Qi C, Goldsby DL and Prior DJ (2017) The down-stress transition from cluster to cone fabrics in experimentally deformed ice. *Earth and Planetary Science Letters* **471**, 136–147.
Ranganathan M, Minchew B, Meyer CR and Peč M (2021) Recrystallization of ice enhances the creep and vulnerability to fracture of ice shelves. *Earth and Planetary Science Letters* **576**, 117219. doi: 10.1016/j.epsl.2021.117219
Reeh N (1968) On the calving of ice from floating glaciers and ice shelves. *Journal of Glaciology* **7**(50), 215–232. doi: 10.3189/S0022143000031014
Rignot E and MacAyeal DR (1998) Ice-shelf dynamics near the front of the Filchner–Ronne ice shelf, Antarctica, revealed by SAR interferometry. *Journal of Glaciology* **44**(147), 405–418. doi: 10.3189/S0022143000002732
Rignot E and 5 others (2004) Accelerated ice discharge from the Antarctic peninsula following the collapse of Larsen B ice shelf. *Geophysical Research Letters* **31**(18), L18401. doi: 10.1029/2004GL020697
Rignot E, Mouginot J and Scheuchl B (2011) Ice flow of the Antarctic ice sheet. *Science* **333**(6048), 1427–1430. doi: 10.1126/science.1208336
Rignot E, Mouginot J and Scheuchl B (2017) Measures InSAR-based Antarctica ice velocity map, version 2.
Rist MA, Sammonds PR, Oerter H and Doake CSM (2002) Fracture of Antarctic shelf ice. *Journal of Geophysical Research: Solid Earth* **107**(B1). ECV 2–1–ECV 2–13. REFDOIdoi: 10.1029/2000JB000058
Robin GdQ (1955) Ice movement and temperature distribution in glaciers and ice sheets. *Journal of Glaciology* **2**(18), 523–532. doi: 10.3189/002214355793702028
Rott H, Rack W, Skvarca P and Angelis HD (2002) Northern Larsen ice shelf, Antarctica: further retreat after collapse. *Annals of Glaciology* **34**, 277–282. doi: 10.3189/172756402781817716
Rudnicki JW (2014) *Fundamentals of Continuum Mechanics*. New Jersey: John Wiley & Sons.
Sandhäger H, Rack W and Jansen D (2005) Model investigations of Larsen B ice shelf dynamics prior to the breakup. *FRISP Report* **16**, 5–12.
Scambos T, Haran T, Fahnestock M, Painter T and Bohlander J (2007) MODIS-based Mosaic of Antarctica (MOA) data sets: continent-wide surface morphology and snow grain size. *Remote Sensing of Environment* **111**(2), 242–257. remote Sensing of the Cryosphere Special Issue. doi: 10.1016/j.rse.2006.12.020
Sergienko OV (2010) Elastic response of floating glacier ice to impact of long-period ocean waves. *Journal of Geophysical Research: Earth Surface* **115**(F4), F04028. doi: 10.1029/2010JF001721
Sergienko OV (2013) Normal modes of a coupled ice-shelf/sub-ice-shelf cavity system. *Journal of Glaciology* **59**(213), 76–80. doi: 10.3189/2013JoG12J096
Sergienko OV (2014) A vertically integrated treatment of ice stream and ice shelf thermodynamics. *Journal of Geophysical Research: Earth Surface* **119**(4), 745–757. doi: 10.1002/2013JF002908
Sergienko OV, Goldberg DN and Little CM (2013) Alternative ice shelf equilibria determined by ocean environment. *Journal of Geophysical Research: Earth Surface* **118**(2), 970–981. doi: 10.1002/jgrf.20054
Seroussi H and 9 others (2020) ISMIP6 Antarctica: a multi-model ensemble of the Antarctic ice sheet evolution over the 21 st century. *The Cryosphere Discussions* **2020**, 1–54.
Shadwick EH and 8 others (2013) Glacier tongue calving reduced dense water formation and enhanced carbon uptake. *Geophysical Research Letters* **40**(5), 904–909. doi: 10.1002/grl.50178
Smith RA (1976) The application of fracture mechanics to the problem of crevasse penetration. *Journal of Glaciology* **17**(76), 223–228. doi: 10.3189/S0022143000013563
Tada H, Paris PC and Irwin GR (2000) *The Stress Analysis of Cracks Handbook, Third Edition*. New York: ASME Press.
Taylor JR (1982) *An Introduction to Error Analysis: The Study of Uncertainties in Physical Measurements*. Sausalito, CA: University Science Books.
Thomas RH and MacAyeal DR (1982) Derived characteristics of the Ross ice shelf, Antarctica. *Journal of Glaciology* **28**(100), 397–412. doi: 10.3189/S0022143000005025
Tyler S and 8 others (2013) Using distributed temperature sensors to monitor an Antarctic ice shelf and sub-ice-shelf cavity. *Journal of Glaciology* **59**(215), 583–591. doi: 10.3189/2013JoG12J207
van den Broeke M (2008) Depth and density of the Antarctic firn layer. *Arctic, Antarctic, and Alpine Research* **40**(2), 432–438.
van der Veen C (1998a) Fracture mechanics approach to penetration of bottom crevasses on glaciers. *Cold Regions Science and Technology* **27**(3), 213–223. doi: 10.1016/S0165-232X(98)00006-8
van der Veen C (1998b) Fracture mechanics approach to penetration of surface crevasses on glaciers. *Cold Regions Science and Technology* **27**(1), 31–47. doi: 10.1016/S0165-232X(97)00022-0
van der Veen CJ (1999) Crevasses on glaciers. *Polar Geography* **23**(3), 213–245. doi: 10.1080/10889379909377677
van Wessem JM and 18 others (2018) Modelling the climate and surface mass balance of polar ice sheets using RACMO2 – part 2: Antarctica (1979–2016). *The Cryosphere* **12**(4), 1479–1498. doi: 10.5194/tc-12-1479-2018
van Wessem JM, van den Broeke MR, Wouters B and Lhermitte S (2023) Variable temperature thresholds of melt pond formation on Antarctic ice shelves. *Nature Climate Change* **13**(2), 161–166.
Vaughan DG (1995) Tidal flexure at ice shelf margins. *Journal of Geophysical Research: Solid Earth* **100**(B4), 6213–6224. doi: 10.1029/94JB02467
Wagner TJW and 8 others (2014) The 'footloose' mechanism: iceberg decay from hydrostatic stresses. *Geophysical Research Letters* **41**(15), 5522–5529. doi: 10.1002/2014GL060832
Wagner TJW, James TD, Murray T and Vella D (2016) On the role of buoyant flexure in glacier calving. *Geophysical Research Letters* **43**(1), 232–240A. doi: 10.1002/2015GL067247
Walker CC, Bassis JN, Fricker HA and Czerwinski RJ (2013) Structural and environmental controls on Antarctic ice shelf rift propagation inferred from satellite monitoring. *Journal of Geophysical Research: Earth Surface* **118**(4), 2354–2364. doi: 10.1002/2013JF002742
Wearing MG (2017) The flow dynamics and buttressing of ice shelves PhD thesis.
Weertman J (1957) Deformation of floating ice shelves. *Journal of Glaciology* **3**(21), 38–42. doi: 10.3189/S0022143000024710
Weertman J (1973) Can a water-filled crevasse reach the bottom surface of a glacier. *IASH Publication* **95**, 139–145.
Weertman J (1974) Depth of water-filled crevasses that are closely spaced. *Journal of Glaciology* **13**(69), 544–544. doi: 10.3189/S0022143000023297
Weertman J (1977) Penetration depth of closely spaced water-free crevasses. *Journal of Glaciology* **18**(78), 37–46. doi: 10.3189/S0022143000021493
Wuite J, Hetzenecker M, Nagler T and Scheiblauer S (2021) ESA Antarctic ice sheet climate change initiative (antarctic_ice_sheet_cci): Antarctic ice sheet monthly velocity from 2017 to 2020, derived from Sentinel-1, v1.
Zarrinderakht M, Schoof C and Peirce A (2022) The effect of hydrology and crevasse wall contact on calving. *The Cryosphere* **16**(10), 4491–4512. doi: 10.5194/tc-16-4491-2022
Zehnder AT (2012) *Fracture Mechanics*, Vol. **62**. London, Dordrecht, Heidelberg, New York: Springer Science & Business Media.
Zeitz M, Levermann A and Winkelmann R (2020) Sensitivity of ice loss to uncertainty in flow law parameters in an idealized one-dimensional geometry. *The Cryosphere* **14**(10), 3537–3550.

Appendix A. Methods for the data-model comparison

To create rift prediction maps, several important steps must be made to ensure sensible and causal predictions. First, we must validate that the areas containing rifts are in regions that largely obey the 1-dimensional (1D) extensional background flow assumptions of the fracture theories assessed in this study. To do so, we use automatic differentiation to construct strain rate fields based on MEaSUREs ice shelf velocity data (Rignot and others, 2011; Mouginot and others, 2012, 2017a; Rignot and others, 2017).

To determine if the 1D fracture theory assumptions are upheld, we utilize the criterion that the normalized resistive stress difference between that of the SSA solution and that assuming 1D flow is within 10%,

$$\left|\frac{\bar{R}_{xx}^{\mathrm{SSA}} - \bar{R}_{xx}^{\mathrm{1D}}}{\bar{R}_{xx}^{\mathrm{1D}}}\right| \leq 0.1, \tag{A1}$$

https://doi.org/10.1017/jog.2024.52 Published online by Cambridge University Press

where $\bar{R}_{xx}^{\mathrm{SSA}} = \bar{B}\dot{\epsilon}_e^{-1+(1/n)}(2\dot{\epsilon}_{xx} + \dot{\epsilon}_{yy})$ and $\bar{R}_{xx}^{\mathrm{1D}} = 2\bar{B}\dot{\epsilon}_{xx}^{1/n}$. This equation can be simplified and written in terms of dimensionless measures of strain rate,

$$\left|\left(1+\alpha^2+\alpha+\xi^2\right)^{1/(2n)-(1/2)}\left(1+\frac{\alpha}{2}\right)-1\right| \leq 0.1, \tag{A2}$$

where the first term with $\alpha = \dot{\epsilon}_{yy}/\dot{\epsilon}_{xx}$ and $\xi = \dot{\epsilon}_{xy}/\dot{\epsilon}_{xx}$ comes from the second invariant of the strain rate tensor under the 3D incompressible condition and assumption of negligible vertical shear stresses. Thus, while one could calculate the depth-averaged ice hardness $\bar{B}(T)$ assuming some vertical temperature profile, this is unnecessary as this term cancels and does not appear in Eqn (A2). Figure 8 shows the region which satisfies the criterion (A2), from which we may select our rifts.

Second, the rifts identified by Walker and others (2013) in these regions must have their thickness values padded to an estimate of the unbroken state thickness. These rifts are currently filled with a conglomerate ice material composed of sea ice, snow and ice shelf fragments, collectively termed as ice mélange in Rignot and MacAyeal (1998); MacAyeal and others (1998); Hulbe and others (1998). Since our goal is to predict if the observed rift could have formed, rather than the stability of the mélange in the rift, we need to estimate the state of the unbroken ice. Here, we generate bounding boxes around rifts of interest and infill the mélange thickness with an average of the local unbroken ice thickness in BedMachine Version 2 (Morlighem, 2020; Morlighem and others, 2020), as shown in Figure 9. Combined with the map of regions that uphold the 1D extensional flow assumption of our fracture theories in Figure 8, we generate rift prediction maps in Figures 6 and 10.

The caveat to this method is that in the absence of remotely sensed data on the time-dependent evolution of basal crevasses into rifts, strain rates and temperature profiles at the time of the basal crack to rift transition remain unknown. We present an analysis of time series data in Appendix B, but these data are largely unavailable for many existing rifts. As such, we utilize the modern values of surface temperatures and strain rates from van Wessem and others (2018) and Wearing (2017), acknowledging that these may have changed since rift formation. We note that the $1/n$ exponent dependence of strain rate given Glen's flow law in Eqn (3) shields the resistive stress from strain rate changes, thus decreasing the sensitivity to precise strain rate estimates.

Due to the uncertainty associated with the temperature and strain rate evolution since the time of rift formation, we construct datasets of stress estimates on the non-rift ice shelf regions, as shown in Figure 11. The advantage of these datasets is that they do not have the time-evolution problem of rift datasets. Therefore, given our methods, we have more confidence in a theory that correctly predicts many rifts and minimally overpredict rifts than a theory which correctly predicts most or all rifts while overpredicting rifts in non-rift regions. In our work, this emphasizes that LEFM with depth-averaged resistive stress result in Zarrinderakht and others (2022) has too low of a threshold for rift initiation.

We note that since Walker and others (2013) do not necessarily identify all rifts in their rift catalog, there could be rifts included in our non-rift region datasets. To help remove rifts not classified by Walker and others (2013) in the non-rift regions of Figure 11, we exclude data that would unanimously be predicted a rift in every fracture theory presented in this study. As such, we take the highest stress threshold for rifting in the Zero Stress approximation with isothermal depth-averaged resistive stress, $\bar{R}_{xx}^{*}/\bar{R}_{xx}^{IT} = 2$. This is reflected in the magnitude of the color bar of Figure 11.

Appendix B. Temporal observation of a basal crevasse to rift transition

Figures 1c,e show the ratio of depth-averaged resistive stress to isothermal ice tongue resistive stress $\bar{R}_{xx}/R_{xx}^{IT}$ over Pine Island Ice Shelf in January and May 2019 respectively. The resistive stress was found using Eqn (7) with along-flow strain rates estimated from 200 × 200 m resolution, monthly averaged ice velocity observations made using feature tracking applied to Sentinel-1 image pairs (Wuite and others, 2021) (https://cryoportal.enveo.at/data/). The strain rate components were calculated via numerical differentiation of the easting and northing velocities using methods developed in Chartrand (2017). Estimates of ice shelf thickness were according to BedMachine version 2 by Morlighem (2020), and the temperature profile was assumed to be linear between −2 °C at the ice shelf base and temperature given by RACMO (van Wessem and others, 2018) at the surface. The accompanying satellite images shown in (d) and (f) are geocoded, multi-looked and radiometrically terrain-corrected Single-Look Complex backscatter data from the European Space Agency and European Commission Copernicus' Sentinel-1 satellites – shown at 50 m resolution.

These show the concurrent evolution of the ratio of stresses near the terminus of the ice shelf alongside the evolution of a rift, likely from a central basal crevasse as argued by Jeong and others (2016), that eventually led to the calving of the B49 iceberg in February 2020. We see clear changes to the along-flow strain rates over the rift as it widens and propagates laterally. This provides a motivating example for determining stress conditions under which basal crevasses transition into rifts, such as those discussed in this article. However, Figures 1c,e show that we measure stress ratios below those required for full-thickness rifts according to each of the theories discussed in this article. That is, the stress ratio over the rift that is clearly visible by May 2019 (Fig. 1f) is below the value of 1 predicted by the Zero Stress approximation, modified to maintain horizontal force balance (Eqn (24)). However, Figure 1 should not be seen as an example aimed at validation of one of the theories considered here, merely as motivation for the work. In part, this is because the central part of Pine Island Ice Shelf does not conform to the assumption of one-dimensional flow (Eqn (A2)) (though the speed of the ice tongue varies little laterally, the flow is dominated by advection and across-flow strain rates are similar in magnitude to along-flow strain rates), nor is the ice shelf cavity necessarily hydrostatic with temperature $T = -2$ °C. Additionally, by using satellite-derived measures of ice velocity averaged over monthly intervals, we cannot hope to capture the maximum strain rates over a crevasse of this scale as the data are too limited in both spatial and temporal resolution. In the future, a validation of the theories discussed in this article using time series of strain rate or stress data should be carried out with the use of higher-resolution satellite data or data collected on the

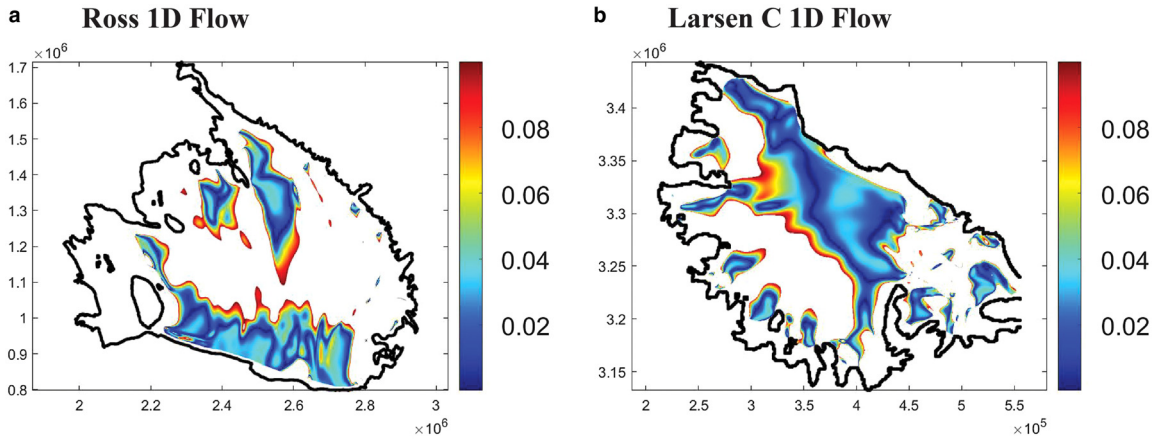

Figure 8. Regions where the background viscous ice flow is approximately 1D based on Eqn (A2). Rifts in these regions are regarded as having formed due to 1D tension, called Mode I failure. The color scale is dimensionless strain rate deviation from 1D flow as in Eqn (A2), and the axes are in units of meters.

https://doi.org/10.1017/jog.2024.52 Published online by Cambridge University Press

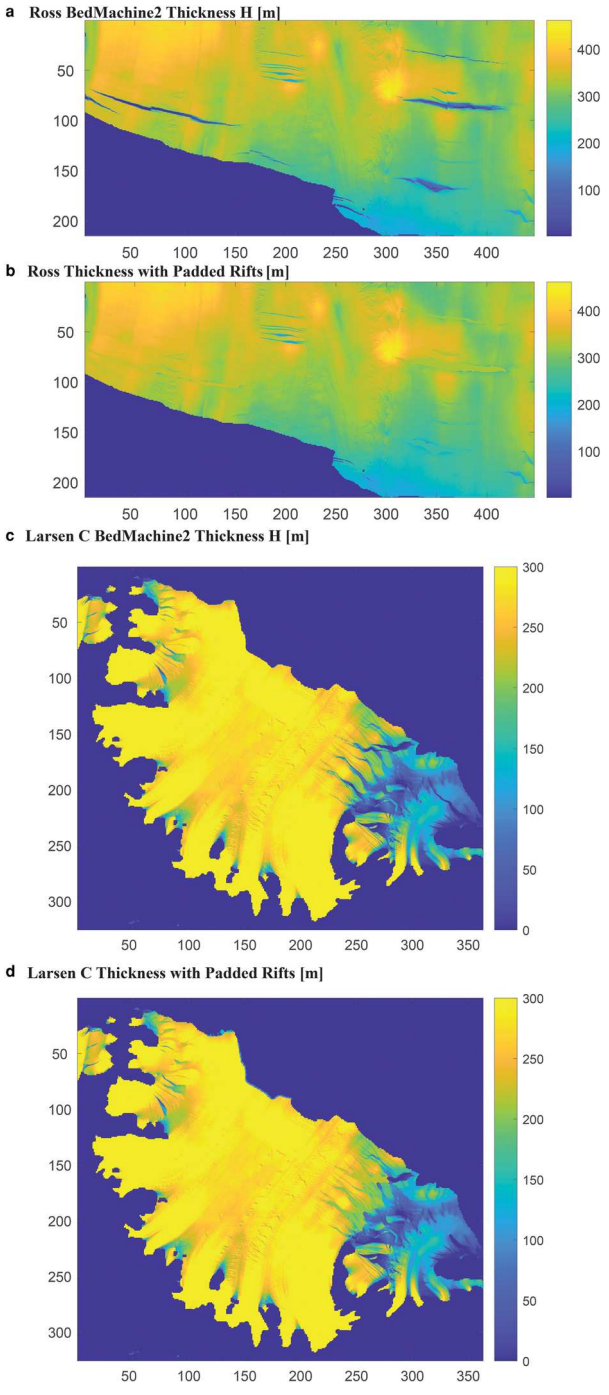

Figure 9. Mélange padding in kilometers with local, unbroken ice thickness on the RIS and LCIS. Subfigures (a) and (c) are the original data products from BedMachine2, while subfigures (b) and (d) are the mélange-padded results used in this study to see if fracture theories can correctly predict rifts in areas where they are known to have occurred. LCIS thickness has an upper bound of 300 m in the color bars of subfigures (c) and (d) to enhance the visibility of padded rifts.

ground, e.g. with the use of an ApRES system as in Nicholls and others (2015). Similarly, it is not possible to accurately determine when the crevasse transitioned into a rift from satellite images alone, or whether it was ever a basal crevasse at all. Future work that aims to use time series data should do so in conjunction with other datasets that provide further information on the type of crevasse under consideration.

Appendix C. Zero stress for rift formation via surface and basal crevasses

The Zero Stress approximation argues that a vertical crack will propagate so long as there is no net compression of the net longitudinal stress σ_n at the crack tip defined in Eqn (1). Written mathematically, the Zero Stress condition ($\sigma_c = 0$) claims that a crack propagates when

$$\sigma_n \geq \sigma_c. \tag{C1}$$

Under the Zero Stress approximation, a basal and surface crevasse will form a rift when the criterion (C1) holds for all depths.

The depth of surface and basal crevasses that result from this Zero Stress condition (C1) are available in the literature (Nye, 1955; Jezek, 1984; Benn and others, 2007; Nick and others, 2010; Duddu and others, 2020),

$$d_s^0 = \frac{R_{xx}}{\rho_i g}, \quad d_b^0 = \frac{R_{xx}}{(\rho_w - \rho_i)g}. \tag{C2}$$

The criterion (C1) can also be re-written in terms of a dimensionless resistive stress, with $z = 0$ at the bottom of the ice,

$$\frac{R_{xx}(z)}{(\rho_w - \rho_i)gH} \geq \begin{cases} \frac{z}{H} & 0 \leq \frac{z}{H} \leq \frac{\rho_i}{\rho_w} \quad \text{(below sea level)} \\ \frac{\rho_i}{\rho_w - \rho_i}\left(1 - \frac{z}{H}\right) & \frac{\rho_i}{\rho_w} \leq \frac{z}{H} \leq 1 \quad \text{(above sea level)} \end{cases} \tag{C3}$$

as visualized by the red dotted lines in Figure 12, which shows basal crevasse depth and rift formation with a linear temperature profile modifying the resistive stress $R_{xx}(z)$.

Since the Zero Stress approximation has zero material strength, the minimum required resistive stress to form a rift is defined by Eqn (C3). If the resistive stress is not in net tension at the ice shelf base, no basal crevasse is predicted. If the resistive stress is in net tension at the base but becomes less than the dotted red curve in Figure 12 at a larger height $z > 0$, the point of equality below sea level is the basal crevasse depth. For example, if the resistive stress takes the value shown by the dashed green line of Figure 12, a basal crevasse would propagate up to a depth about 60% of the unbroken ice thickness. However, resistive stresses that are greater than or equal to the dotted red curve for all heights will form rifts because basal crevasses can propagate all the way to the surface. Figure 12 clearly demonstrates the underestimation of rifts when depth-averaged resistive stress theories, the dashed lines, are used instead of their depth-dependent counterparts, the solid curves.

Next, we develop the mathematical expression for the rift initiation stress threshold of the Zero Stress approximation. These expressions are plotted in dashed blue and solid green in Figures 7 and 16. Taking the assumption that the second invariant of strain rate is approximately the along-flow strain rate for consistency with LEFM, the rift formation criterion given isothermal, depth-averaged resistive stress can be written as a dimensionless stress ratio,

$$\frac{\bar{R}_{xx}}{\bar{R}_{xx}^{IT}} \geq 2, \tag{C4}$$

with $\bar{R}_{xx}^{IT} = (1 - \rho_i/\rho_w)\rho_i g H/2$ the depth-averaged ice tongue resistive stress. This equation can be understood visually from Figure 12 as the corner of the dotted red curve located on the x-axis at $R_{xx}/\left((\rho_w - \rho_i)gH\right) = \rho_i/\rho_w \approx 0.89$, which is equivalent to (C4). Similarly, in the depth-dependent case, we have that

$$\frac{\bar{R}_{xx}}{\bar{R}_{xx}^{IT}} \geq 2\frac{\rho_w}{\rho_i}\frac{d_b^*}{H}\frac{\bar{\tilde{B}}(T)}{\tilde{B}(T(\frac{d_b^*}{H}))}. \tag{C5}$$

Here $\tilde{B}(T) = B(T)/B(T = -2\ ^\circ\text{C})$ is the dimensionless ice hardness, $\bar{\tilde{B}}(T)$ is the depth-averaged dimensionless ice hardness, and d_b^* is the unstable basal crevasse depth at which a basal crevasse will propagate to form a rift. The unstable basal crevasse depth d_b^* depends upon temperature profile and the prescribed stresses. For isothermal ice, the unstable basal crevasse height is sea level without tides, $d_b^* = H\rho_i/\rho_w$, and we also have that $\bar{\tilde{B}}(T) = \tilde{B}(T(d_b^*/H))$, so the above Eqn (C5) reduces to the depth-averaged case in Eqn (C4). For vertical temperature profiles that become colder toward the ice shelf surface, the unstable basal crevasse depth d_b^* can decrease. Given the ice hardness function of LeB Hooke (1981) and a linear temperature profile from $T_b = -2\ ^\circ\text{C}$ at the base, the unstable basal crevasse depth d_b^* falls below sea level for surface temperatures at least as cold as $T_s = -25\ ^\circ\text{C}$ in the Zero Stress theory as well as HFB, as shown with the blue curves of Figure 4a with $T_s = -32\ ^\circ\text{C}$.

https://doi.org/10.1017/jog.2024.52 Published online by Cambridge University Press

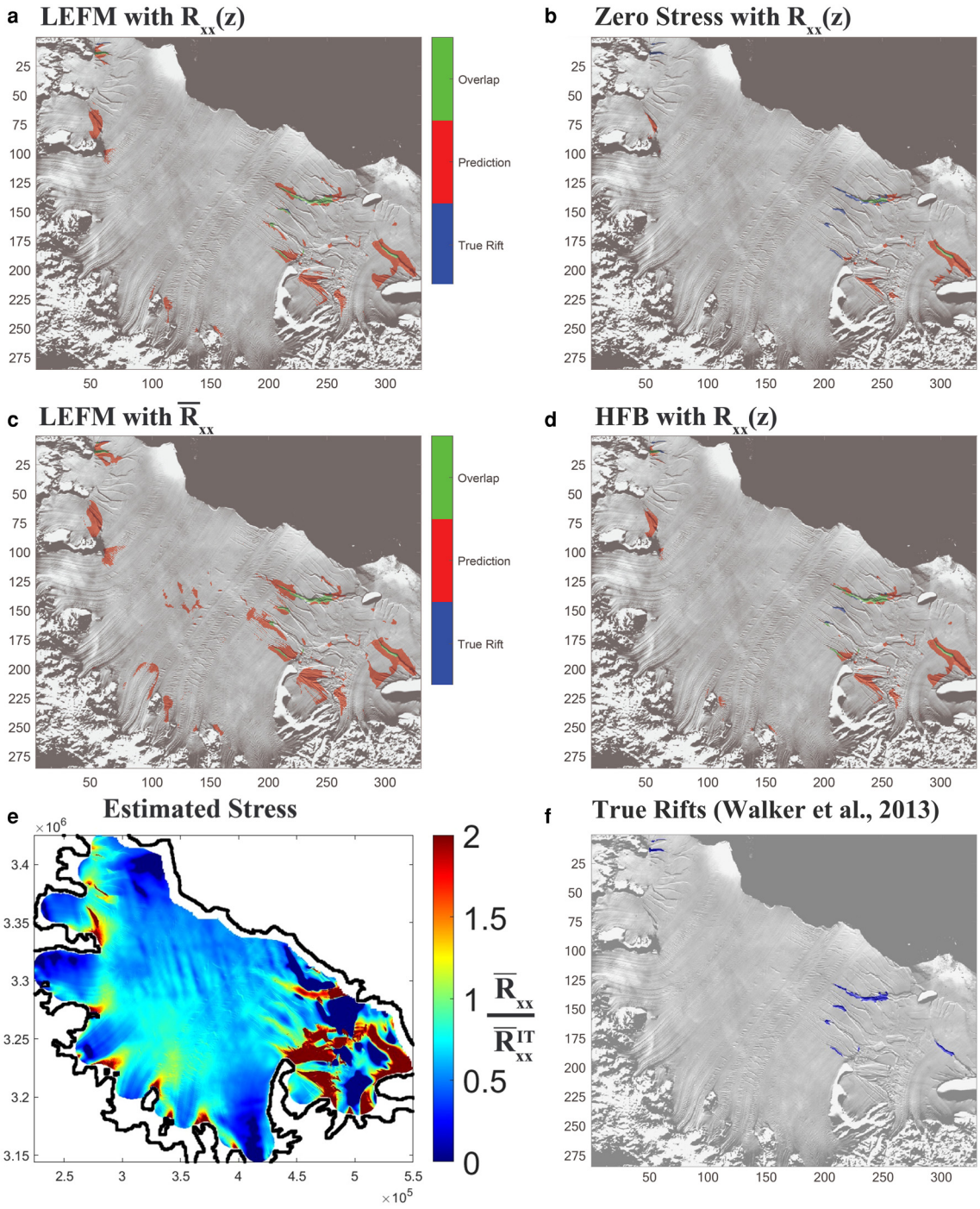

Figure 10. Same as Figure 6, except on LCIS, assuming a linear temperature profile.

Appendix D. Temperature dependence of linear elastic fracture mechanics for ice shelf basal crevasses

In this Appendix section, we first explain the stability of LEFM basal crevasses given (1) and (6), and then the effects of ice-shelf temperature on crack depth and rifting stress, as shown in Figure 4c.

D.1. LEFM basal crack stability

Figure 13 indicates the possible solutions for LEFM through increasing the resistive stress, similar to presentation in Lai and others (2020). In the blue curve, we see that the stress intensity factor is less than the fracture toughness for all crack depths, implying no fracture could exist for that given resistive stress. For a larger resistive stress (red curve), a tangent solution exists where the stress intensity factor is equal to the fracture toughness, so a stable crack exists, but it cannot propagate. This crack depth is the maximum initial flaw size required to form a stable crack. Following (Lai and others, 2020), the maximum initial flaw size is $\kappa(K_{Ic}/(\rho_i g))^{2/3} \approx 15$ m for a basal crevasse, with $\kappa \approx 2.27$, $K_{Ic} = 0.15$ MPa·m$^{1/2}$ from Litwin and others (2012), $\rho_i = 917$ kg m^{-3} and $g = 9.8$ m s^{-2}. For an even larger resistive stress, an initial flaw (open circle) would propagate as long as $K_I \geq K_{Ic}$, potentially finding a stable crack depth, as shown by the solid circle on the yellow curve. Finally, there exists a rifting stress $\bar{R}^*_{xx}$ above which initial flaws would unstably propagate through the entire ice thickness, as shown by the purple curve.

Below, we discuss the dependence of LEFM results on vertical temperature profile in terms of (1) stable crevasse depths and (2) the rifting stress threshold $\bar{R}^*_{xx}$ that corresponds to the first unstable solution.

D.2. Temperature effects on basal crevasse depths and the rifting stress threshold

As shown in our Figure 4c, for the same depth-averaged resistive stress, colder ice has shallower crack depths. This may seem at odds with Figure 3 of van der

https://doi.org/10.1017/jog.2024.52 Published online by Cambridge University Press

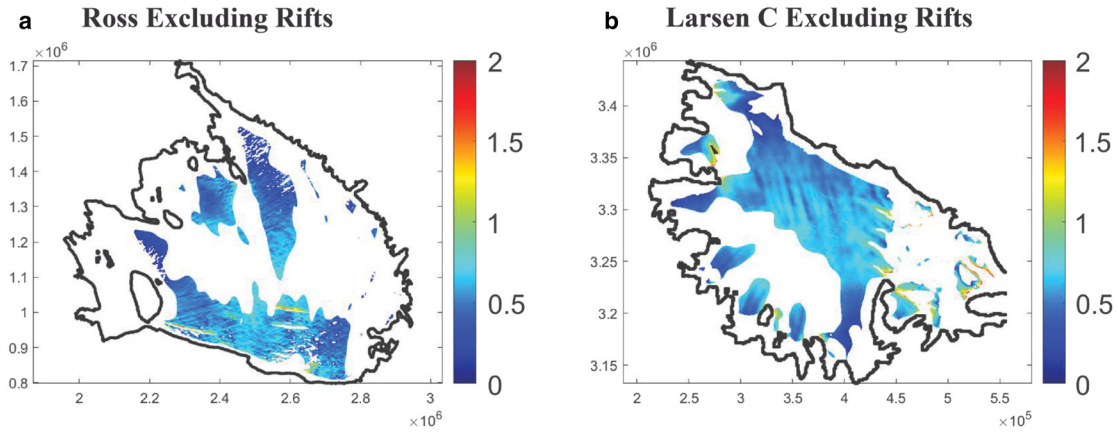

Figure 11. Extensional, approximately 1D regions of RIS and LCIS, assuming a linear temperature profile, that exclude both observed rifts and rifts predicted by a resistive stress greater than twice the freely floating resistive stress. The color shows the magnitude of $\bar{R}_{xx}/\bar{R}_{xx}^{IT}$, and axes are in meters.

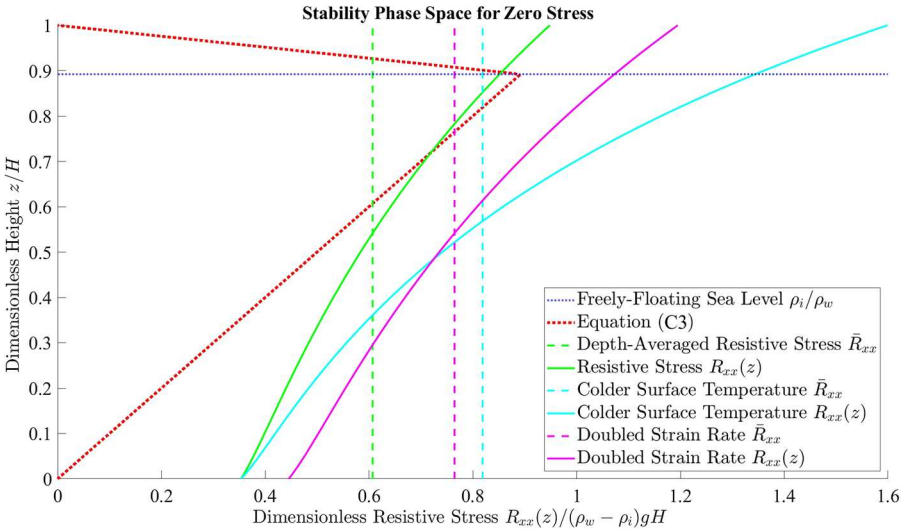

Figure 12. Visualizing the Zero Stress condition. The dotted red curve, defined by the piecewise distribution in Eqn (C3), is the magnitude of the lithostatic pressure minus water pressure that opposes fracture; the intersection below sea level of a given resistive stress with the dotted red curve determines basal crevasse depth. Solid curves utilize $R_{xx}(z)$, whereas dashed lines utilize $\bar{R}_{xx}$. Green curves with surface temperature $T_s = -22$ °C are the reference for cyan and magenta curves; cyan curves utilize $T_s = -32$ °C, and magenta curves have along-flow strain rate doubled. Depth-averaged resistive stresses have unstable basal crevassing occur only at sea level, and may be solved for analytically; vertical temperature profiles may have crevasses unstably propagate before sea level, and require numerical treatment.

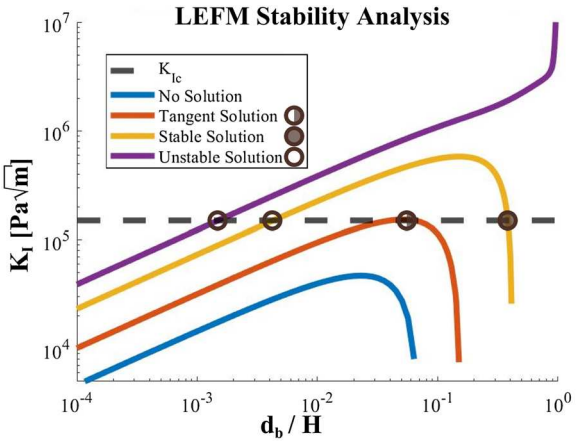

Figure 13. Understanding possible LEFM solutions for isothermal ice with a constant thickness $H = 300$ m and fracture toughness $K_{Ic} = 150$ kPa$\sqrt{m}$ (dashed line). The solid curves are the stress intensity factors from (6) with varying resistive stress. Descriptions of the possible solutions are in the text of this Appendix D.

Veen (1998a) that shows colder ice temperatures promote deeper crack depths. However, it is actually consistent; Figure 3 of van der Veen (1998a) is for a constant strain rate, whereas our Figure 4 is for constant normalized resistive stress. Since the resistive stress depends exponentially on the temperature through the effective viscosity as shown in (2), (3) and (4), colder temperatures will have higher viscosity and thus decreased strain rate for the same value of depth-averaged resistive stress. Thus, for the same depth-averaged resistive stress, colder ice has shallower crack depths.

As shown by the LEFM solutions in Figure 4c that turn toward vertical as d_b goes to H; there is an unstable basal crevasse depth d_b^* at which rifts are formed, similar to the other theories in this study. Since $d_b^* < H$ is when rifting is determined, and $\int_0^{d_b} (\bar{R}_{xx} - R_{xx}(z))dz$ increases for colder surface temperatures given a monotonically decreasing temperature profile toward the ice surface, the diverging rifting stress between the depth-averaged resistive stress $\bar{R}_{xx}$ and vertically varying resistive stress $R_{xx}(z)$ is expected, as shown in Figure 7.

Appendix E. Derivation of horizontal force balance

Here we demonstrate how the Zero Stress approximation does not uphold horizontal force balance on an isothermal ice shelf through an Eulerian control volume argument based on Buck (2023), also see Section 2.3. The main argument of the control volume approach, as has been applied by Weertman (1957) and Jezek (1984) to solve for the net tension we call $\bar{R}_{xx}^{IT}$ at ice fronts, is Newton's Second Law. The sum of the forces acting on the control volume are equal to the product of mass and acceleration of fluid entering the control volume. In our case, there is no net acceleration of fluid into or out of the control volume, and the shear stresses on surface and bottom boundaries are negligible. Thus, we can write the horizontal force balance for a control volume between a crevassed location $x = x_c$ and an uncrevassed downstream location $x = x_c + \Delta x$ as

$$\int_0^H [\sigma_{xx}(x_c + \Delta x, z) - \sigma_{xx}(x_c, z)]dz = 0. \quad \text{(E1)}$$

https://doi.org/10.1017/jog.2024.52 Published online by Cambridge University Press

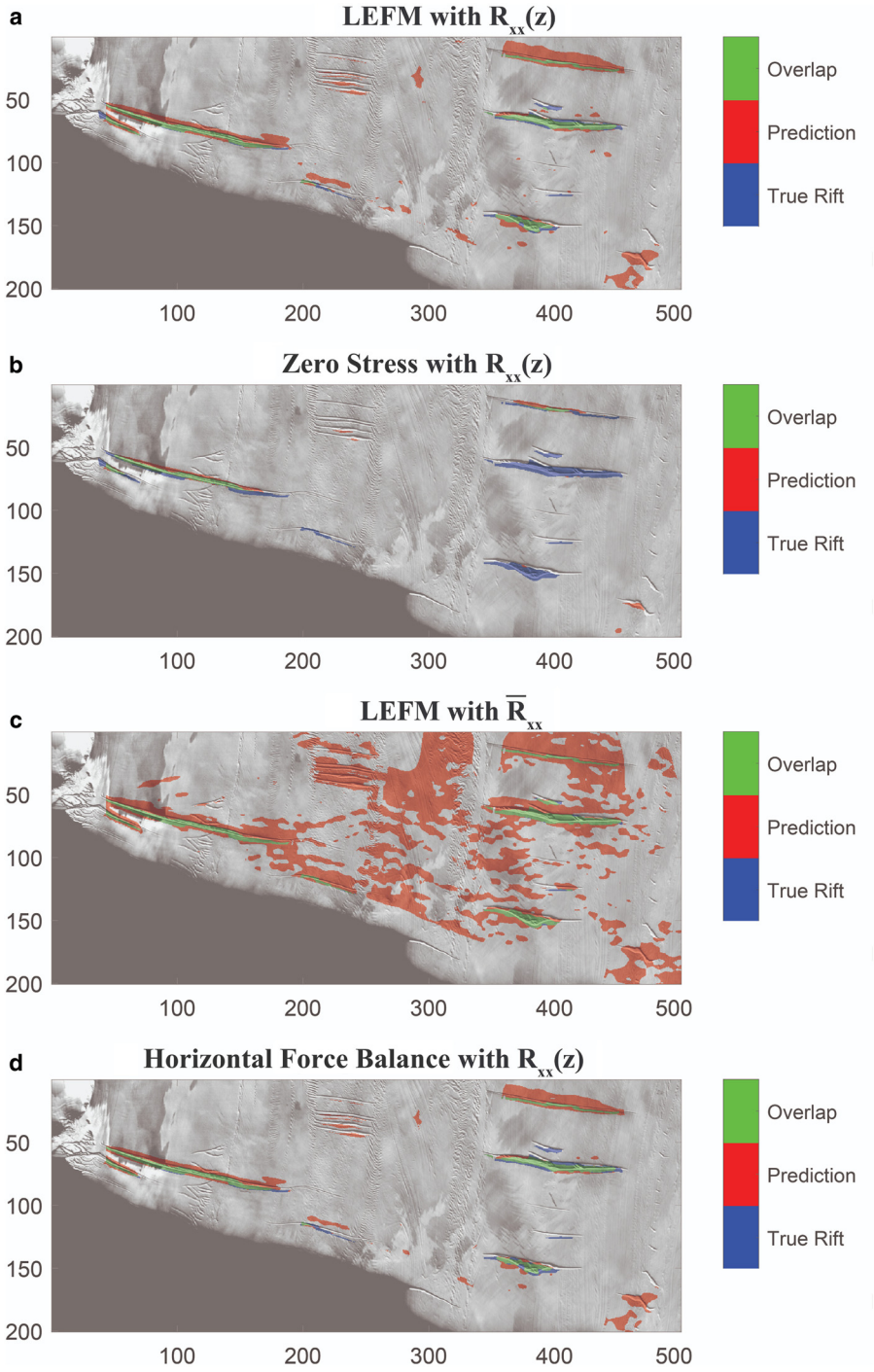

Figure 14. The same map view plot in kilometers as Figure 6, except that a Robin temperature profile is taken to generate the rift formation stresses and assumed in calculating the value of stress in the data.

The horizontal force balance model for an isothermal ice shelf was developed in Buck (2023) and is summarized below. At the downstream location $x = x_c + \Delta x$ that is sufficiently far away from the bending stresses near the ice front (Reeh, 1968; Wagner and others, 2016), we have

$$\sigma_{xx}(x_c + \Delta x, z) = -\rho_i g(H - z) + R_{xx}(x_c + \Delta x). \tag{E2}$$

At the crevassed location, we will follow the Zero Stress assumption and have dual surface and basal crevasses with depths d_s and d_b,

$$\sigma_{xx}(x_c, z) = \begin{Bmatrix} 0, & H - d_s \le z \le H \\ -\rho_i g(H - z) + R_{xx}(x_c) & d_b \le z \le H - d_s \\ -\rho_w g(z_h - z), & 0 \le z \le d_b \end{Bmatrix}. \tag{E3}$$

Note that the stresses cannot be the same at both locations, or $\sigma_{xx}(x = x_c) \neq \sigma_{xx}(x = x_c + \Delta x)$, because the intact ice is effectively thinner at the crevassed location. If we were to evaluate the force balance of Eqn (E1) with the incorrect assumption of $\sigma_{xx}(x = x_c) = \sigma_{xx}(x = x_c + \Delta x)$, the crack depths would be twice as deep as that of the Zero Stress theory,

$$d_s = \frac{2R_{xx}}{\rho_i g},\ d_b = \frac{2R_{xx}}{(\rho_w - \rho_i)g}, \tag{E4}$$

and the stress distribution at the surface crevasse tip would not be continuous, $\sigma_{xx}(z = H - d_s) = -\rho_i g\ d_s + R_{xx} \neq 0$. Thus, to satisfy a continuous stress at the surface crack tip, we have

$$R_{xx}(x = x_c) = \rho_i g d_s. \tag{E5}$$

Similarly, using stress continuity at the basal crack tip gives a relation between

https://doi.org/10.1017/jog.2024.52 Published online by Cambridge University Press

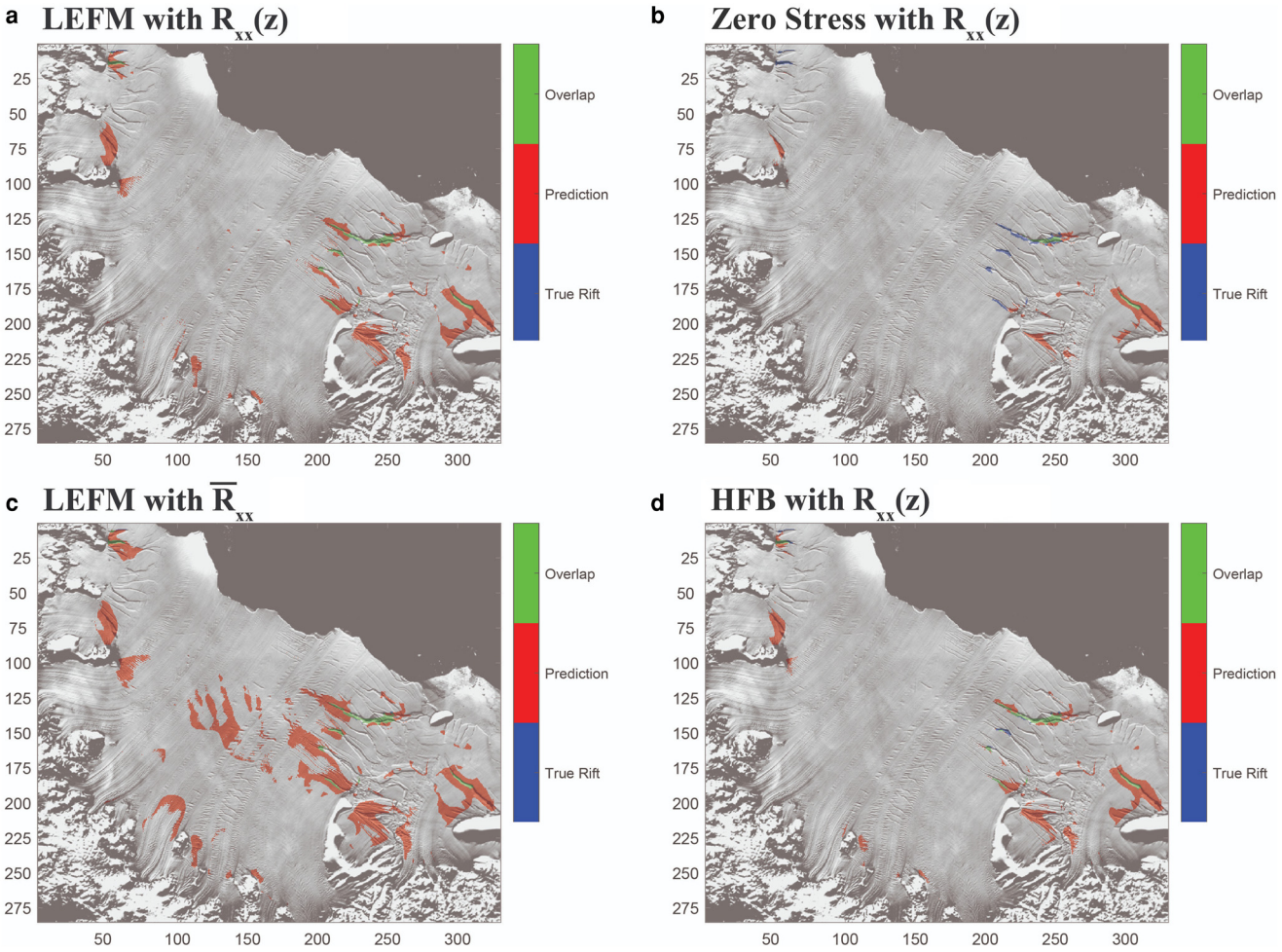

Figure 15. Following Figure 14, we use the same concept as Figure 10, except that a Robin temperature profile is used to generate the rift formation stresses and assumed in calculating the stress values of the data. Axes are in kilometers.

surface and basal crack depths,

$$(\rho_w - \rho_i)d_b = \rho_i d_s. \tag{E6}$$

With the crack depth relation in Eqn (E6), plugging the stress definitions in Eqns (E2), (E3), (E5) into the force balance condition of Eqn (E1) yields the analytical crack depth predictions of Buck (2023) for an isothermal ice shelf,

$$\begin{aligned} \frac{d_b}{H} &= \frac{\rho_i}{\rho_w}\left(1 - \sqrt{1 - \frac{R_{xx}(x_c + \Delta x)}{\bar{R}_{xx}^{IT}}}\right), \\ \frac{d_s}{H} &= \left(1 - \frac{\rho_i}{\rho_w}\right)\left(1 - \sqrt{1 - \frac{R_{xx}(x_c + \Delta x)}{\bar{R}_{xx}^{IT}}}\right). \end{aligned} \tag{E7}$$

For more insight into the role of temperature dependence, we now specify the form of Eqns (19) and (20) for a simplified, approximate ice hardness function and linear vertical temperature profile. In Eqn (4), the second term in the brackets, $-C/(T_r - T)^k$, is two to three orders of magnitude smaller than the first term, T_0/T. Similarly, with temperature $T(\tilde{z}) = T_b[1 - (1 - T_s/T_b)\tilde{z}]$ in Kelvin, the term $(1 - T_s/T_b)\tilde{z}$ is at least an order of magnitude smaller than unity, so we may Taylor expand the exponent to first order in $(1 - T_s/T_b)\tilde{z}$. We define the approximated ice hardness function B_a with these two simplifications,

$$B_a(T(\tilde{z})) \approx B_0 \exp\left[\frac{T_0}{T_b + (T_s - T_b)\tilde{z}}\right] \approx B_0 \exp\left[\frac{T_0}{T_b}\right] \exp\left[\frac{\tilde{z}}{\tilde{z}_0}\right], \tag{E8}$$

with the dimensionless e-folding length scale $\tilde{z}_0 \equiv ((T_0/T_b)(1 - T_s/T_b))^{-1}$.

Therefore, the crevasse depth relation of Eqn (19) may be written as

$$\tilde{d}_b = \tilde{d}_s \frac{\rho_i}{\rho_w - \rho_i} \exp\left[\frac{-(1 - \tilde{d}_s - \tilde{d}_b)}{\tilde{z}_0}\right], \tag{E9}$$

and the horizontal force balance of Eqn (20) may be written as

$$\begin{aligned} \frac{\bar{R}_{xx}}{\bar{R}_{xx}^{IT}} = {} & \frac{\rho_w}{\rho_w - \rho_i}\tilde{d}_s^2 + \frac{\rho_w}{\rho_i}\tilde{d}_b^2 \\ & + \frac{\tilde{d}_s}{\frac{1}{2}\left(1 - \frac{\rho_i}{\rho_w}\right)}\tilde{z}_0\left(1 - \exp\left[\frac{-(1 - \tilde{d}_s - \tilde{d}_b)}{\tilde{z}_0}\right]\right). \end{aligned} \tag{E10}$$

Even with the simplified ice hardness, these equations (E9) and (E10) are not algebraically solvable due to the nature of the Arrhenius equation. Although the result including vertically varying temperature requires numerical treatment, the rift initiation stress threshold produced using LeB Hooke (1981)'s ice hardness function is within 0.1% of the analytical isothermal solution $R_{xx}^*/\bar{R}_{xx}^{IT} = 1$ for all surface temperatures used for both linear and Robin temperature profiles. Therefore, we can well-approximate the rift initiation stress threshold as that of a freely floating ice shelf without buttressing, i.e.

$$\frac{\bar{R}_{xx}^*}{\bar{R}_{xx}^{IT}} = 1. \tag{E11}$$

Appendix F. Result robustness: uncertainty estimation

A discussion of result robustness is incomplete without considering the uncertainty in data products. The largest data uncertainty comes from the measurements of ice thickness (Morlighem, 2020; Morlighem and others, 2020), where

https://doi.org/10.1017/jog.2024.52 Published online by Cambridge University Press

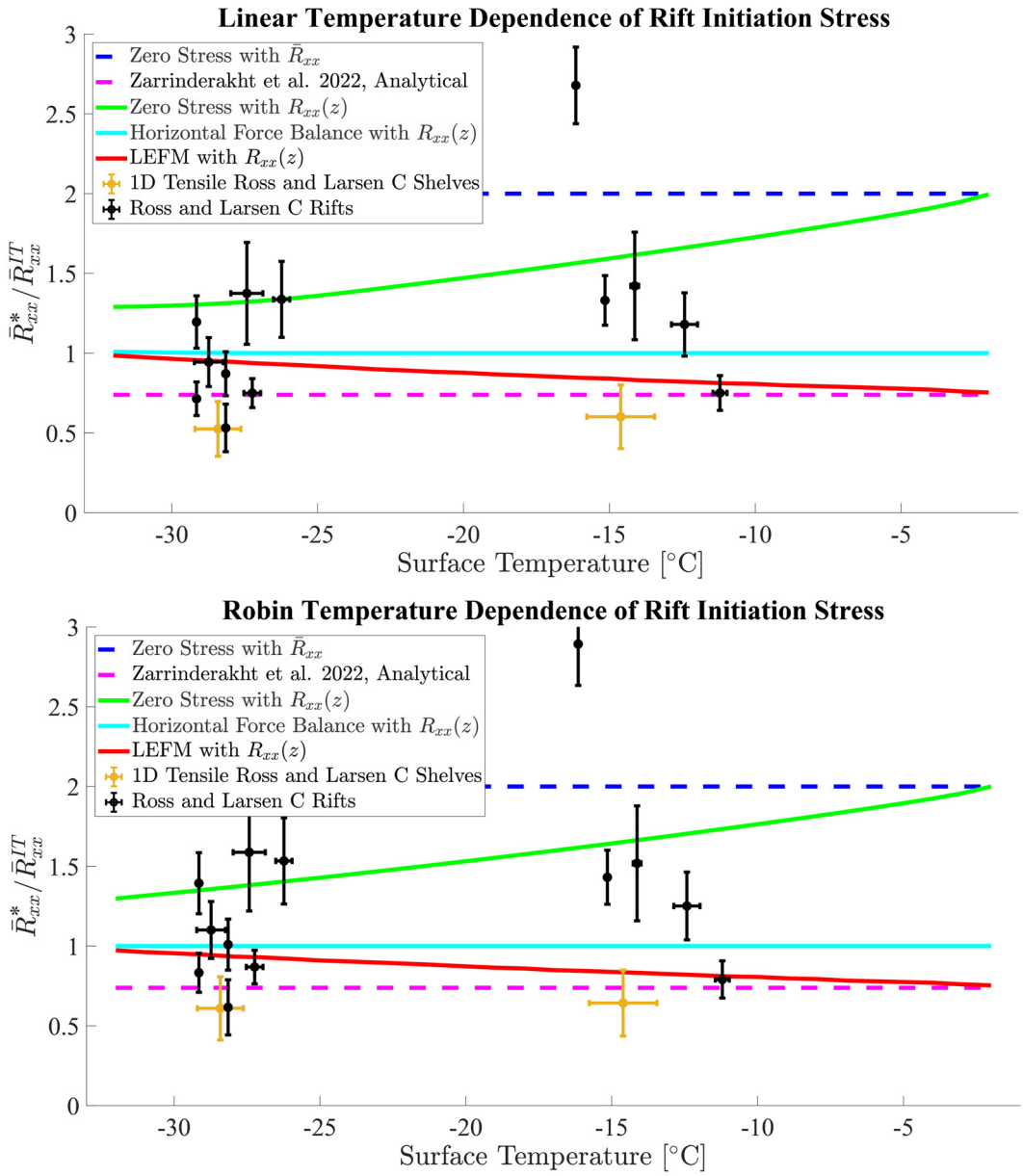

Figure 16. The same idea as Figure 7, except that we include approximate rift stress data and evaluate linear and Robin temperature profiles for generating the depth-dependent rift formation stresses (green, cyan and red curves). Relative to the linear temperature profile, the Robin profile raises the value of the resistive stresses in the rifts and non-rift ice shelf datasets (black and orange data, respectively), but has a negligible effect on the rifting stress threshold curves. Horizontal Force Balance is a much more accurate rift initiation theory compared with the Zero Stress approximation, and is largely or fully insensitive to surface temperature assuming a linear or Robin profile. This provides robustness, as the same conclusions are drawn with either a linear or Robin temperature profile.

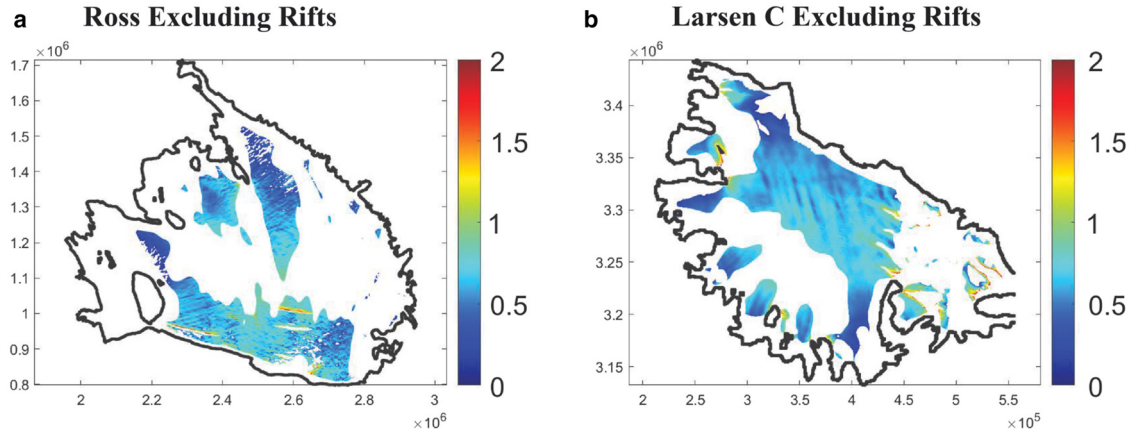

Figure 17. The same as Figure 11, except that the Robin temperature profile raises the value of the depth-averaged resistive stress relative to the linear temperature profile. Axes are in meters.

https://doi.org/10.1017/jog.2024.52 Published online by Cambridge University Press

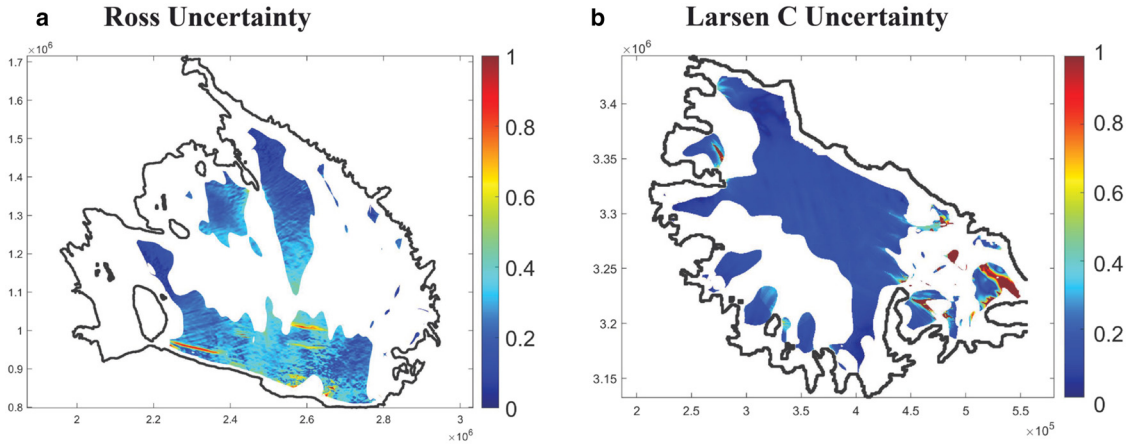

Figure 18. Estimates of dimensionless resistive stress uncertainty σ_β defined in Eqn (F2) on RIS and LCIS, with thickness padded for known rifts. The small uncertainty on LCIS provides more confidence in our work. The color scale is capped at $\sigma_\beta = 1$, as there are a few outliers due to thickness uncertainty being comparable or larger than ice thickness. Axes are in meters.

the uncertainties in our regions of interest are 100 m for the majority of the RIS, or around a third of the ice thickness, and around 30 m for the LCIS, or about a tenth of the ice thickness. Alone, one standard deviation of this uncertainty would shift the data points up or down by about a third for RIS data or about a tenth for LCIS data on Figures 7 and 16. As such, we look at LCIS for result robustness. Importantly, if the ice shelf data of interest is governed by the 1D SSA momentum equation (MacAyeal, 1989),

$$\frac{\mathrm{d}}{\mathrm{d}x}\left(H\bar{R}_{xx}\right) = \rho_\mathrm{i} g H\left(1 - \frac{\rho_\mathrm{i}}{\rho_\mathrm{w}}\right)\frac{\mathrm{d}H}{\mathrm{d}x}, \tag{F1}$$

then the depth-averaged resistive stress scales linearly with H. To compute uncertainty accurately for dependent variables, we would have to use covariance (Taylor, 1982); however, we cannot meaningfully compute the covariance for each pixel of ice shelf data, and so we estimate the upper bound on uncertainty σ_β with

$$\sigma_\beta \leq \sqrt{\sum_i \left(\frac{\partial \beta}{\partial x_i}\sigma_{x_i}\right)^2} = \beta\sqrt{\left(\frac{\sigma_H}{H}\right)^2 + \left(\frac{\sigma_{\dot{\epsilon}_{xx}}}{n\dot{\epsilon}_{xx}}\right)^2 + \left(\frac{\partial B(T^*)}{\partial T^*}\frac{\sigma_{T^*}}{B(T^*)}\right)^2}. \tag{F2}$$

Here, our variable of interest is the dimensionless resistive stress $\beta = \bar{R}_{xx}/\bar{R}_{xx}^{IT}$. The uncertainties in thickness, strain rate and equivalent temperature are σ_H, $\sigma_{\dot{\epsilon}_{xx}}$ and σ_{T^*}, with equivalent temperature T^* defined as the temperature at which $\bar{B} = B(T^*)$ (Sergienko, 2014). We take the strain rate uncertainty associated with 20 km from the ice front from Table C.1 of Wearing (2017) and apply this to the whole ice shelf. Given that we do not have defined uncertainties associated with equivalent temperature, we estimate $\sigma_{T^*} = 3$ K from the uncertainty range associated with modeled and observed RACMO surface temperature data in Figure 3a of van den Broeke (2008). In this calculation, we assume the Robin temperature profile in our ice hardness and equivalent temperature calculations, as we do not expect profiles warmer than linear, but this choice is negligible in the final results.

We plot the upper bound of dimensionless resistive stress uncertainty σ_β in Figure 18. Given the distributions of these datasets have some large outliers that skew the mean, we report the estimated median uncertainties for RIS and LCIS are $\sigma_\beta = 0.27$ and $\sigma_\beta = 0.14$, respectively. The RIS median uncertainty is large as anticipated, and the LCIS median uncertainty is comparable to the difference between LEFM with $R_{xx}(z)$ and Horizontal Force Balance given the temperatures on LCIS (see red and cyan curves in Figs 7, 16). Therefore, more precise measurements of ice thickness, strain rate and temperature are needed to further observationally constrain the optimal theory for tensile rift initiation from basal crevasses.

https://doi.org/10.1017/jog.2024.52 Published online by Cambridge University Press